



Bachelor's Diploma Thesis
Department of Applied Mathematics
University of Crete

Imaging of extended reflectors in two-dimensional waveguides.

Symeon Papadimitropoulos

Advisors: Prof. Chrysoula Tsogka
Dr. Dimitris Mitsoudis

Heraklion, October 2012

Acknowledgements

A lot of people deserve to be on this page, each for separate reasons. First of all, my supervisors, Chrysoula Tsogka and Dimitrios Mitsoudis, that gave me the opportunity, through this work, to expand my mathematical horizons and, of course, for their ongoing support throughout the course of this work.

I could not neglect to thank the post-doctoral associate and colleague Adrien Semin for his invaluable help and the endless hours spent in order to resolve any technical difficulties that occurred.

At this point, I would also like to thank the members of the thesis examination committee, Georgios Makrakis and Michael Plexousakis for their time and input regarding the thesis report.

Before the end, I would like to thank my family for their unlimited support, emotional and financial, but mostly for the faith they had in me throughout all these years.

Contents

	Page
1 Introduction	1
2 Wave propagation in waveguides	5
2.1 Description of the problem	5
2.2 Mathematical formulation	9
2.2.1 The wave equation	9
2.2.2 The Helmholtz equation	10
2.2.3 The Green's function	11
2.3 Array imaging setup	13
3 Imaging	15
3.1 Introduction	15
3.2 Imaging in Waveguides	18
3.2.1 Resolution Analysis	20
3.3 Selective Imaging	25
3.4 Modal Projection and selective imaging	26
4 Numerical Simulations	29
4.1 Description of the numerical method	29
4.2 Implementation	31
4.3 Numerical Results	32
5 Analysis of the imaging method	39
5.1 Array response matrix	40
5.2 Selective imaging	45

5.3	Comparison	48
5.3.1	$\tilde{\mathcal{I}}_J^{KM}$ vs. asymptotics	48
5.3.2	\mathcal{I}_J^{KM} vs. $\tilde{\mathcal{I}}_J^{KM}$	52
5.3.3	Full object vs. crack	54

Chapter 1

Introduction

In this work we consider the problem of detecting and imaging *extended* reflectors submerged in the sea, using acoustic waves. The first step lies in emitting a sound pulse from a source and letting the wave propagate through the medium. It will then interact with the reflectors (if any are present) and we will record the acoustic pressure field along an array of receivers. The recorded data can then be used to create an image, thus enabling us to estimate the position of the reflector as well as some of its characteristics. The term *extended* refers to reflectors which are comparable in size to the acoustic wavelength. In our case, the sea will be modeled as an acoustic waveguide consisting of a single homogeneous water layer confined above by the sea surface and below by the seafloor, both of which are assumed to be horizontal; thus our waveguide is an infinite strip of constant depth.

The imaging problem that we wish to solve can be described as follows: The extended reflector is illuminated by a vertical array which spans the whole depth of the waveguide. Each array element can act both as a source and a receiver. By emitting a pulse from each element of the array and recording the field on all receivers, we create a matrix, that we shall call the *array response matrix*. Next, we define a search domain (a bounded subset of our waveguide) and with the recorded acoustic pressure field as our data, we want to create an image of the search domain, which will hopefully illustrate the presence or absence of the scatterer, its position etc. This is achieved by computing and plotting the values of appropriate imaging func-

tionals, which have the property that their values within the search domain with the smallest deviation from zero, represent the lack of any perturbation in the medium, while the largest values indicate the presence of a perturbation. Examples of such imaging functionals include the *Kirchhoff migration functional* (see [3, §9]) and the *matched field functional* (see [14]).

Another question that many times arises in imaging is whether we can create an image which focuses on specific parts of the scatterer. One way to achieve this, is to use a *selective imaging* technique called the subspace projection method (cf. [4]). This method, is based on the singular value decomposition (SVD), see for example [9, §2.5], of the array response matrix, which helps us to create a filtered version of it which, in turn, will be used for imaging purposes. In [4], the extended scatterer was embedded in a homogeneous medium while in [6] the authors considered selective imaging in clutter, *i.e.*, propagation media with inhomogeneities that are unknown, cannot be estimated in detail, and, are modeled as random processes.

The concept of selective imaging of extended scatterers has been motivated by the concept of *selective focusing*, which concerns the case where there are multiple point (or small) scatterers in the medium and, essentially, allows one to distinguish specific scatterers by creating an image which focuses on them. In this direction, the work of Prada and Fink [18] has been very influential. They have introduced the so-called DORT method (DORT is an acronym for ‘decomposition of the time reversal operator’ in French), which uses the singular value decomposition of the time reversal operator to focus selectively on scattering obstacles. The experimental results obtained in [18] show that for small scatterers, the number of nonzero (or significant) singular values of the response matrix is exactly the number of obstacles contained in the medium. Furthermore, the use of the corresponding singular vectors as incident field results in selective focusing on the scatterers, provided that these are located sufficiently far from each other. Related works include [19, 17]. When the scatterers are clustered together, the one-to-one correspondence between the singular vectors of the response matrix and the scatterers does not hold any more, and as a consequence, selective focusing cannot be achieved with DORT. This problem was addressed in [5] where selective focusing was achieved by using as illumination an optimal convex

combination of the leading singular vectors across the bandwidth. To the best of our knowledge, the first rigorous mathematical justification of DORT has been given in [12], where the propagation medium is the free space \mathbb{R}^3 . For the analysis of DORT in a waveguide environment we refer to the analysis done by Pinçon and Ramdani [16].

The main goal of the present work is to examine the behavior of imaging functionals when selective imaging techniques are used in order to focus in different parts of our object (in our case the object is a single extended scatterer) submerged in a homogeneous two-dimensional waveguide with horizontal boundaries. Moreover, we would like to derive a relation between the number of significant singular values of the response matrix and the reflector's size.

Relevant works in the same spirit, but for the free space case, include [21], where an analysis of the response matrix for extended reflectors is presented, and [4], where the behavior of the imaging functionals with selective imaging techniques has been analyzed and a relation between the number of significant singular values and the size of the reflector has been proven.

This work is organised as follows. In Chapter 2, we formulate our problem and present the basic theory concerning wave propagation in waveguides. We discuss the equations that describe the propagation of the acoustic field in time and frequency domains. We also introduce relevant terminology commonly used in imaging, such as the active array and the array response matrix.

Next, in Chapter 3 we discuss the main features of the imaging problem in general setups and, also, for our specific waveguide environment. We present the imaging functionals that will be used throughout this work and we perform a resolution analysis for the case of a *point* scatterer submerged in our waveguide. At the end of the chapter, an alternative imaging functional, based on the projection of the response matrix on the propagating modes, is introduced and details about the concept of selective imaging are given.

In Chapter 4, we present the outcome of our numerical experiments in the case where the extended scatterer is a rigid square. The data which are necessary in order to form the array response matrix are created numerically by solving the wave equation in the waveguide, with and without the

scatterer, using a high-order finite element C++ code, called Montjoie [1]. Montjoie has been developed in INRIA and is very effective in solving equations that arise in wave propagation problems. At the end of the chapter, we present imaging results produced by the standard imaging functional and the projected one, when selective imaging techniques are applied.

Lastly, in Chapter 5 we present a theoretical analysis of the imaging method for a simplified model problem where the scatterer is a crack, *i.e.*, a vertical one-dimensional perfect reflector. For this model problem, we derive a relation between the number of significant singular values of the array response matrix and the size of our scatterer. This result is, to the best of our knowledge, a new one concerning a waveguide geometry. We also explore the form of the singular vectors of the response matrix in order to gain some insight regarding the selective imaging features. In the last section we compare theoretical and numerical results for the simplified model where the scatterer is a crack and, also, results for the crack and the full scatterer.

Chapter 2

Wave propagation in waveguides

2.1 Description of the problem

In this work we consider the problem of detecting and imaging *extended* scatterers submerged in the sea, using acoustic waves. The first step, lies in emitting a sound pulse from a source and letting the wave propagate through the medium. It will then interact with the scatterers (if any are present) and we will record the acoustic pressure field along an array of receivers. The recorded data can then be used to create an image, thus enabling us to estimate the position of the scatterer, as well as some of its characteristics. Note that the term *extended* refers to scatterers which are comparable in size to the acoustic wavelength. Scatterers much smaller than the wavelength are usually called point scatterers.

The ocean is usually modeled as an acoustic waveguide confined above by the sea surface and below by the seafloor; this waveguide behavior is evident particularly in shallow water regions. A schematic representation of a marine waveguide model is shown in Figure 2.1. Other typical examples of waveguides, are ducts, optical fibers, etc.

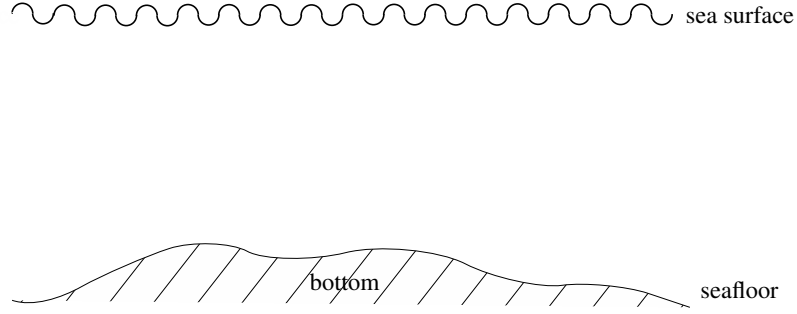


Figure 2.1: Schematic representation of a marine waveguide.

The marine acoustic environment is, in general, very complicated: the sound speed is usually non uniform, the sea surface is a rough, time-dependent surface, the ocean seafloor is a very complex rough boundary, and the bottom is typically a complicated, layered medium which supports elastic waves. In the water layer, the sound speed depends, mainly, on the temperature, salinity and pressure (which is a function of depth). In many cases the sound speed may be calculated with sufficient accuracy using the following semi-empirical formula, [20],

$$c = 1449.2 + 4.6 T - 0.055 T^2 - 0.00029 T^3 + (1.34 - 0.010 T)(S - 35) + 0.016 x,$$

where c is the sound speed in m/s, T is the temperature of the water in $^{\circ}\text{C}$, S is the salinity of the water in parts per thousand and x is the depth in meters.

In our case we will assume that the waveguide is two-dimensional and consists of a single homogeneous water layer, which translates to a constant wave speed throughout the waveguide and, also, that the surface and the seafloor are horizontal; thus our waveguide is an infinite strip of constant depth D , as shown in Figure 2.2. Note that, as usually happens in underwater acoustics applications, the depth x is taken positive downwards, while, here, z denotes the range variable. Of course, this problem, known as the *isovelocity problem* (see [13, §5.4]), is ideal and simplified, but still exhibits the main characteristics of acoustic wave propagation in the sea and many of its properties may carry over to more general setups.



Figure 2.2: Schematic representation of our simplified waveguide model.

The acoustic pressure field generated by some source and recorded when the wave propagates through the medium, is called the *incident field*. Under the above assumptions, we shall see later that it is possible to have a closed-form expression for the incident field generated by a point-source. In the presence of a scatterer in the medium, the recorded field is then called the *total field*. If we know the total and the incident field and subtract the incident field from the total field, we get what we call the *scattered field*, *i.e.*, the field that describes only the reflections of the wave from the scatterer.

When dealing with the scattering of acoustic waves from an object, we may distinguish the scatterers in *penetrable* and *impenetrable*. For example, very often the following cases are studied:

- a. The scatterer is *acoustically soft* and impenetrable, in which case the acoustic pressure vanishes on its boundary. Such a scatterer is modeled by imposing a homogeneous Dirichlet condition for the total field on the boundary of the scatterer.
- b. The scatterer is *acoustically hard* and impenetrable. In this case, the total field satisfies a homogeneous Neumann condition on the boundary of the scatterer.
- c. In the case where the scatterer is a penetrable object filled with a fluid which has different values for the density and sound speed than those in the rest of the medium, one should impose appropriate transmission conditions on its boundary.

In this work we will focus on the imaging of extended, *acoustically hard*, *impenetrable* scatterers. More specifically, we will deal with the so-called

active array imaging problem, which may be briefly summarized as follows. We have an array of sources, an array of receivers and a scatterer placed in the medium. The sources emit acoustic waves and the receivers record the produced field which will be used to create our images. There are two setups, depending on the location of the source and receiver arrays, which are common in active array imaging: a) The *transmission* problem, where the scatterer is located between the source and the receiver arrays, as shown in Figure 2.3,

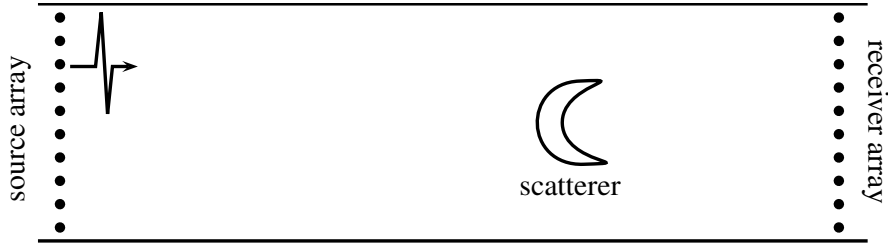


Figure 2.3: Transmission problem geometry.

and b) the *reflection* problem, where both arrays are on the same side of the scatterer, as shown in Figure 2.4. This terminology originates in medical imaging, where, usually, the array geometry varies depending on the problem. Here, we will deal with the reflection problem and, specifically, we will have a single vertical array consisting of *transducers* which act both as sources and receivers.

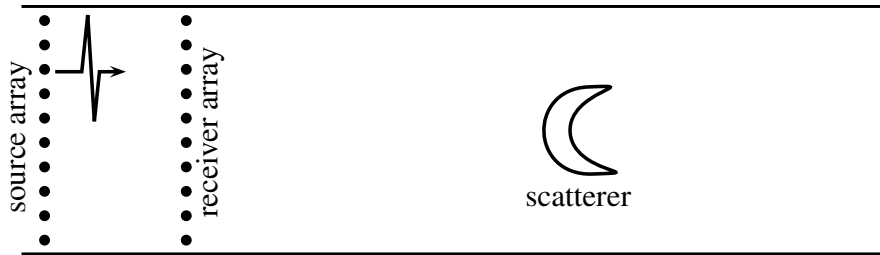


Figure 2.4: Reflection problem geometry.

The propagation of the acoustic field in the waveguide is governed by the scalar acoustic wave equation, which is briefly discussed in the next section.

2.2 Mathematical formulation

2.2.1 The wave equation

The propagation of sound in homogeneous media is described by the wave equation

$$\frac{\partial^2 p}{\partial t^2}(t, \vec{x}) - c^2 \Delta p(t, \vec{x}) = f(t, \vec{x}), \quad (2.1)$$

where $f(t, \vec{x})$ is a forcing term.

In order to obtain unique, physically meaningful solutions of the wave equation in the waveguide of Figure 2.2, we must supplement (2.1) with appropriate initial, boundary and radiation conditions.

On the surface, we impose a pressure-release condition, *i.e.* a homogeneous Dirichlet boundary condition. On the bottom, in most cases, we will pose a homogeneous Neumann boundary condition to simulate a rigid bottom. In some cases, we will use a homogeneous Dirichlet boundary condition to simulate an acoustically soft bottom and take advantage of the properties coming from the symmetry of the problem in this case. The radiation condition describes our physical intuition that sources with compact support produce outgoing, radiating wave fields at infinity. Under these conditions, the following problem is formulated for the incident field,

$$\left\{ \begin{array}{l} \frac{\partial^2 p^{inc}}{\partial t^2}(t, \vec{x}) - c^2 \Delta p^{inc}(t, \vec{x}) = f(t, \vec{x}), \quad \vec{x} = (z, x) \in \mathbb{R} \times [0, D], \quad t \geq 0, \\ p^{inc}(0, \vec{x}) = f(0, \vec{x}), \quad \vec{x} \in \mathbb{R} \times [0, D], \\ p^{inc}(t, z, 0) = 0, \quad t \geq 0, \quad z \in \mathbb{R}, \\ p^{inc}(t, z, D) = 0, \text{ or } \frac{\partial p^{inc}}{\partial n}(t, z, D) = 0, \quad t \geq 0, \quad z \in \mathbb{R}, \\ p(t, \vec{x}) \text{ is outgoing as } z \rightarrow \infty, \end{array} \right. \quad (2.2)$$

where n is the outward unit normal vector. In the presence of an extended, acoustically hard scatterer in the medium occupying a domain \mathcal{O} , the total field satisfies

$$\left\{ \begin{array}{l} \frac{\partial^2 p^{tot}}{\partial t^2}(t, \vec{x}) - c^2 \Delta p^{tot}(t, \vec{x}) = f(t, \vec{x}), \quad \vec{x} = (z, x) \in \mathbb{R} \times [0, D], \quad t \geq 0, \\ p^{tot}(0, \vec{x}) = f(0, \vec{x}), \quad \vec{x} \in \mathbb{R} \times [0, D], \\ p^{tot}(t, z, 0) = 0, \quad t \geq 0, \quad z \in \mathbb{R}, \\ p^{tot}(t, z, D) = 0 \text{ or } \frac{\partial p^{tot}}{\partial n}(t, z, D) = 0, \quad t \geq 0, \quad z \in \mathbb{R}, \\ \frac{\partial p^{tot}}{\partial n}(t, z, x) = 0, \text{ on } \partial\mathcal{O}, \quad t \geq 0, \quad (z, x) \in \partial\mathcal{O}, \\ p(t, \vec{x}) \text{ is outgoing as } z \rightarrow \infty. \end{array} \right. \quad (2.3)$$

The problem for the incident field (2.2) can be solved analytically, while, for scatterers of arbitrary geometry (2.3) needs to be solved numerically. We will describe later the numerical method that we will use to solve (2.3). Another alternative is to take the Fourier transform of (2.2) with respect to time and solve the resulting Helmholtz equation in the frequency domain.

2.2.2 The Helmholtz equation

Let us assume that the term f represents the effect of a source which emits a time-harmonic signal of angular frequency ω and harmonic time dependence of the form $e^{i\omega t}$, where i is the imaginary unit.

In this case, by applying the Fourier transform to equation (2.1) with respect to time, we obtain a new partial differential equation

$$\Delta \hat{p}(\omega, \vec{x}) + \frac{\omega^2}{c^2} \hat{p}(\omega, \vec{x}) = \hat{f}(\omega, \vec{x}), \quad (2.4)$$

where $\hat{p}(\omega, \vec{x})$ is the Fourier transform of the acoustic pressure

$$\hat{p}(\omega, \vec{x}) = \int_{-\infty}^{+\infty} p(t, \vec{x}) e^{i\omega t} dt,$$

and $\hat{f}(\omega, \vec{x})$ the Fourier transform of the source term $f(t, \vec{x})$

$$\hat{f}(\omega, \vec{x}) = \int_{-\infty}^{+\infty} f(t, \vec{x}) e^{i\omega t} dt.$$

Equation (2.4) is known as the Helmholtz equation. A significant advantage of the Helmholtz equation over the wave equation, is the reduction in the dimension.

2.2.3 The Green's function

Of particular importance for the solution of the inhomogeneous Helmholtz equation with a source \hat{f} , is the consideration of point sources represented by the Dirac delta function $\delta(\vec{x} - \vec{x}_s)$, where $\vec{x}_s = (z_s, x_s)$ is the source location. In Cartesian coordinates (z, x) , this function becomes

$$\delta(\vec{x} - \vec{x}_s) = \delta(z - z_s)\delta(x - x_s).$$

The solution of (2.4) with point source forcing of unit strength, supplemented by the boundary and radiation conditions described before, is called the Green's function of the acoustic waveguide and is denoted by $\hat{G}(\vec{x}; \vec{x}_s)$. It is the incident field due to a point source located at \vec{x}_s . In order to compute the Green's function, we have to solve

$$\Delta \hat{G}(\vec{x}; \vec{x}_s) + k^2 \hat{G}(\vec{x}; \vec{x}_s) = \delta(\vec{x} - \vec{x}_s), \quad (2.5)$$

where $k = \omega/c$ is the wavenumber, subject to appropriate boundary conditions.

Specifically, here we assume a homogeneous Dirichlet boundary condition on the surface ($x = 0$) and a homogeneous Neumann boundary condition on the bottom ($x = D$).

Then a (formal) solution to this problem may be written in the form

$$G(z, x) = \sum_{n=1}^{\infty} Z_n(z) X_n(x), \quad (2.6)$$

where X_n are the orthonormal eigenfunctions and λ_n the associated eigenvalues of the one-dimensional Sturm-Liouville problem

$$\begin{cases} X''(x) + \lambda X(x) = 0, \\ X(0) = 0, \quad X'(D) = 0, \end{cases} \quad (2.7)$$

$$i.e., \lambda_n = \left(\frac{(n-1/2)\pi}{D} \right)^2, \quad X_n = \sqrt{\frac{2}{D}} \sin(\sqrt{\lambda_n}x), \quad n = 1, 2, \dots \quad (2.8)$$

Henceforth we will assume that there exists an index M such that

$$\lambda_M < k^2 < \lambda_{M+1}. \quad (2.9)$$

In other words, we assume that the *number of propagating modes* in the waveguide is M .

We substitute (2.6) into (2.5) and we get that

$$\begin{aligned} \sum_{n=1}^{\infty} (X_n'' Z_n + Z_n'' X_n + k^2 X_n Z_n) &= -\delta(x - x_s) \delta(z - z_s) \\ \Rightarrow \sum_{n=1}^{\infty} (Z_n'' + (k^2 - \lambda_n) Z_n) X_n &= -\delta(x - x_s) \delta(z - z_s). \end{aligned}$$

We multiply the relation above by $X_m(x)$ and integrate with respect to x from 0 to D to get

$$\sum_{n=1}^{\infty} (Z_n'' + (k^2 - \lambda_n) Z_n) \int_0^D X_n(x) X_m(x) dx = -\delta(z - z_s) \int_0^D \delta(x - x_s) X_m(x) dx. \quad (2.10)$$

Since the eigenfunctions $X_n(x)$ are orthonormal,

$$\int_0^D X_n(x) X_m(x) dx = \delta_{mn},$$

where δ_{mn} is the Kronecker delta and, also,

$$\int_0^D \delta(x - x_s) X_m(x) dx = X_m(x_s).$$

Therefore (2.10) becomes

$$Z_m'' + (k^2 - \lambda_m) Z_m = -\delta(z - z_s) X_m(x_s).$$

Thus we seek a continuous function Z_m whose derivative has a jump of magnitude $X_m(x_s)$ at $z = z_s$. Hence

$$Z_m(z) = \frac{i}{2\beta_m} e^{i\beta_m|z-z_s|} X_m(x_s), \quad (2.11)$$

with

$$\beta_n = \begin{cases} \sqrt{k^2 - \lambda_n}, & n = 1, \dots, M \\ i\sqrt{\lambda_n - k^2}, & n \geq M + 1. \end{cases} \quad (2.12)$$

By using equations (2.8) and (2.11) we have the following expression for the Green's function as an infinite sum of modes

$$\hat{G}(z, x) = \frac{i}{2} \sum_{n=1}^{\infty} \frac{1}{\beta_n} e^{i\beta_n |z - z_s|} X_n(x_s) X_n(x). \quad (2.13)$$

See also [15] for an alternative derivation of (2.13).

2.3 Array imaging setup

As already mentioned, we are working in a two-dimensional waveguide, consisting of a single homogeneous water layer with constant sound speed $c_0 = 1500$ m/s. The waveguide has horizontal boundaries, thus creating an infinite strip of constant depth $D = 200$ m. We are working on a Cartesian coordinate system (z, x) , where z is the range variable and x the depth, conventionally taken positive downwards. In this work the scatterers will be considered to be acoustically hard and square shaped, with side lengths that are multiples of the wavelength λ , *e.g.* $b = \lambda, 2\lambda, \dots$

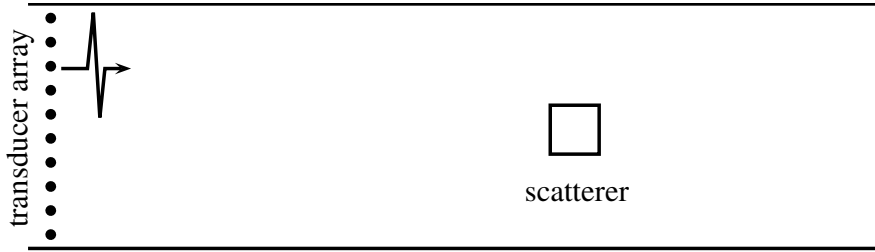


Figure 2.5: Schematic representation of a waveguide with a scatterer.

On the left side of the scatterer, there is a vertical array consisting of $N = 39$ equidistant transducers, with a *pitch* (interelement array distance) of $h = 5$ m. Each source emits an acoustic pulse and all the receivers record the produced field.

By emitting a pulse from each element of the array and recording the field on all the receivers, we create the *array response matrix*, denoted by

$\Pi(t)$ ($\hat{\Pi}(\omega)$ in the frequency domain). Each entry $\Pi_{ij}(t)$ of the response matrix, corresponds to the field recorded at a receiver located at \vec{x}_j , due to a source located at \vec{x}_i , at a given time t (for a given frequency ω in the frequency domain), which is

$$\Pi_{ij}(t) = p(t, \vec{x}_j; \vec{x}_i),$$

where $p(t, \vec{x}_j; \vec{x}_i) = p(t, \vec{x}_j)$ is the solution of (2.2) for the incident field (respectively of (2.3) for the total) with a source term of the form

$$f(t, \vec{x}) = \delta(t)\delta(\vec{x} - \vec{x}_i).$$

The array response matrix contains the data we will use for imaging. More precisely, we will use the response matrix corresponding to the scattered field, so we will have to compute the response matrices for the total and incident fields, $\Pi^{tot}(t)$ and $\Pi^{inc}(t)$, respectively, and subtract them to obtain the response matrix for the scattered field,

$$\Pi^{scat}(t) = \Pi^{tot}(t) - \Pi^{inc}(t).$$

Chapter 3

Imaging

3.1 Introduction

The imaging problem that we wish to solve can be described as follows: with the recorded acoustic pressure field as our data, we want to create an image of a specific domain and estimate features such as the number of scatterers, their shape and their acoustical properties.

We can distinguish two main imaging techniques: passive and active array imaging. In the case of passive array imaging we have a source that emits an acoustic pulse, creating an acoustic field that is recorded by an array of receivers and we try to image the source.



Figure 3.1: Passive array imaging setup.

A typical setup in active array imaging assumes, except the arrays of sources and receivers, the presence of one scatterer (or more) in the medium. As mentioned before, in this work we will deal with the active array imaging problem and, more specifically, the reflection problem, where we have one

array consisting of transducers that can act both as sources and receivers (see Figure 3.2).

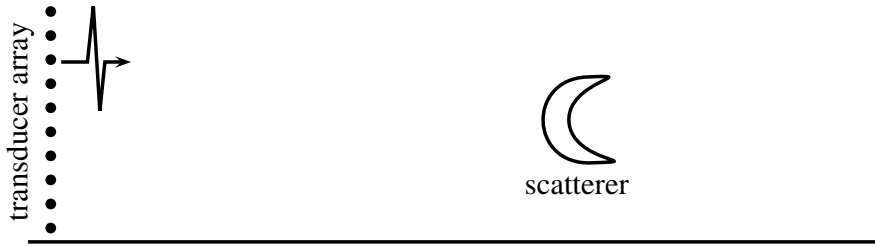


Figure 3.2: Active array imaging setup.

In order to create an image, we first need to determine a search domain \mathcal{D} inside our medium, discretized by points $\vec{y}^s = (z^s, x^s)$, as shown in Figure 3.3.

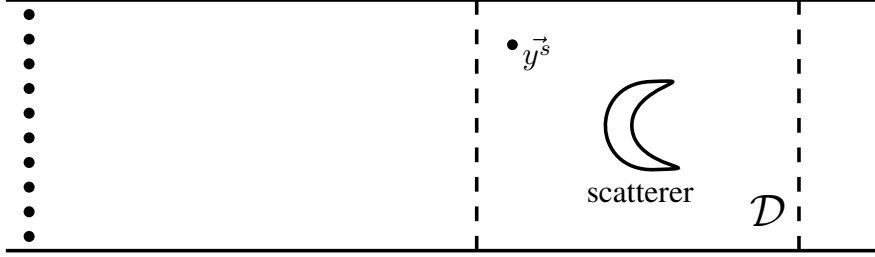


Figure 3.3: A search domain with a scatterer in it.

We would like to define an appropriate imaging functional such that its smallest values within the search domain represent the lack of any perturbation in the medium, while its largest values indicate the presence of a perturbation. Examples of such imaging functionals include the *Kirchhoff migration functional* (see [3, §9]), given by

$$\mathcal{I}^{KM}(\vec{y}^s, \omega) = \sum_{\vec{x}_s, \vec{x}_r} \overline{\hat{G}_0(\vec{x}_r, \vec{y}^s, \omega)} \overline{\hat{G}_0(\vec{y}^s, \vec{x}_s, \omega)} \hat{\Pi}(\vec{x}_r, \vec{x}_s, \omega), \quad (3.1)$$

and the *matched field functional* (see [14]),

$$\mathcal{I}^{MF}(\vec{y}^s, \omega) = \left| \sum_{\vec{x}_s, \vec{x}_r} \overline{\hat{G}_0(\vec{x}_r, \vec{y}^s, \omega)} \overline{\hat{G}_0(\vec{y}^s, \vec{x}_s, \omega)} \hat{\Pi}(\vec{x}_r, \vec{x}_s, \omega) \right|^2. \quad (3.2)$$

In (3.1) and (3.2), bars denote complex conjugation.

In (3.1) and (3.2), \hat{G}_0 is typically a *model* for the Green's function in the propagation medium. We use the word *model*, because in general, we cannot assume that we have perfect knowledge of the background medium and therefore $\hat{G}_0 \neq \hat{G}$ in imaging. For the waveguide problem we chose to define \hat{G}_0 as

$$\hat{G}_0(z, x) = \frac{i}{2} \sum_{n=1}^{\infty} e^{i\beta_n|z-z_s|} X_n(x_s) X_n(x), \quad (3.3)$$

which is practically \hat{G} given by (2.13) where we have omitted the β_n from the denominator. We made this choice because, as we move to the last propagating modes, the β_n tend to 0, and create numerical instabilities when used. The numerical experiments we have performed suggest that omitting the β_n does not affect the resolution of our images.

In (3.1) and (3.2) we define the imaging functionals for a fixed frequency ω . When we have multi-frequency data, we can compute instead,

$$\mathcal{I}^{KM}(\vec{y}^s) = \left| \sum_{\omega} \mathcal{I}^{KM}(\vec{y}^s, \omega) \right|, \quad (3.4)$$

and

$$\mathcal{I}^{MF}(\vec{y}^s) = \sum_{\omega} \mathcal{I}^{MF}(\vec{y}^s, \omega), \quad (3.5)$$

respectively. In this work, we use the Kirchhoff migration functional. The idea behind Kirchhoff migration is the backpropagation of the signals from the source to a point \vec{y}^s in the search domain and then back to the receiver. This process is done for all sources and receivers. If the search point \vec{y}^s is the “origin” where the signal was reflected, then the imaging functional in this position will have a large value, otherwise its value will be small, close to zero. Kirchhoff migration is widely used in seismic imaging and exploration geophysics, applications for which the arrays are very large and so is the bandwidth. This is a setup for which perfect imaging resolution can be achieved. Indeed, in that case the ideal point spread function (*i.e.*, the image of a point scatterer), the Dirac delta distribution, can be obtained at least asymptotically as the array aperture and the bandwidth tend to infinity (cf. [3]). To be more precise the result is obtained for a slight modification of

(3.1) that uses a weighing factor which takes into account the source receiver geometry. In the next section we will study the imaging resolution for KM in a waveguide.

3.2 Imaging in Waveguides

Let us assume that a point scatterer is located somewhere in the waveguide environment described in the previous chapter. As we shall see, the corresponding image for this point scatterer is not a delta function, as one would ideally expect, but some other function, usually called the point spread function. It admits its maximum at the location of the point scatterer and its support determines the *range* and *cross-range* resolution of our image.

The resolution depends on the length of the array, the frequency we use, as well as the bandwidth of the pulse that is emitted. One of the advantages of the waveguide geometry is that rays that would vanish in free space, get reflected on the boundaries of the waveguide and remain in the medium (see Figure 3.4). In this way, we have many more rays that can interact with our scatterer, thus giving us more information about the object.

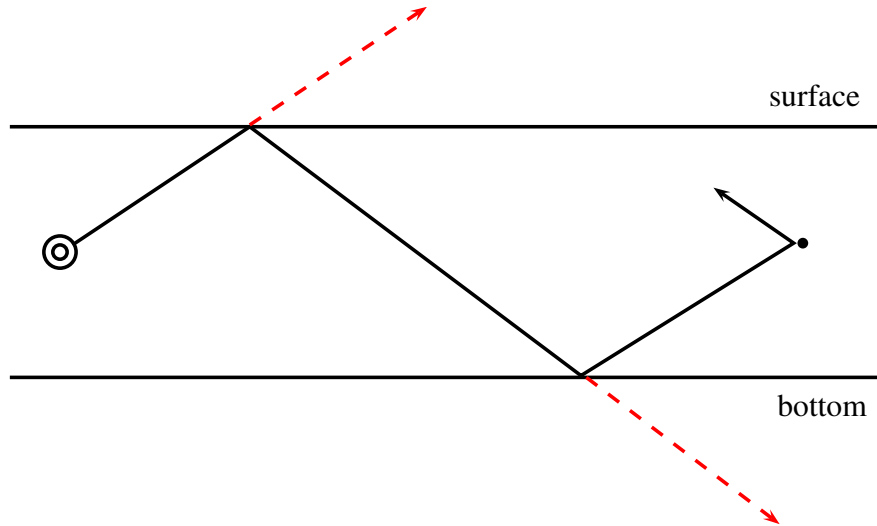


Figure 3.4: A ray travelling in a waveguide. The red dotted lines represent the path the ray would follow if not for the boundaries of the waveguide.

Using the *method of images*, we can show that having an array which

spans the whole depth of the waveguide is equivalent to having an array of infinite length in free space, thus resulting in a much better resolution than if the finite array was placed in free space.

In Figure 3.5, we plot the modulus of the values of $\mathcal{I}^{KM}(\vec{y}^s, \omega)$ (see (3.1)), for points $\vec{y}^s = (z, x)$ in an orthogonal regular grid with a uniform discretization $\Delta x = \Delta z = 2$ m in the search domain $[330, 630] \times [0, 200]$. The waveguide has a rigid bottom, its depth is $D = 200$ m, the sound speed is $c_0 = 1500$ m/s, the frequency is $f_0 = 75$ Hz, so that the wavelength is $\lambda_0 = 20$ m. The small scatterer is a square with side length $b = 10$ m $= \lambda_0/2$ and its center is placed at $(480, 80)$ m. Note that in the computation of \hat{G}_0 we have taken into account just the 20 propagating modes.

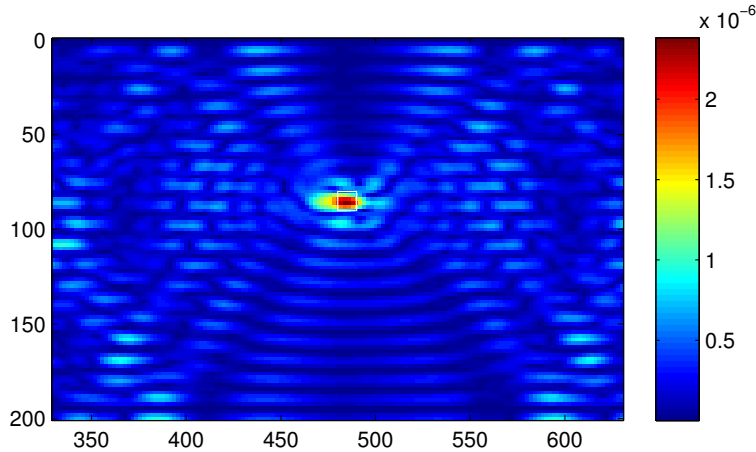


Figure 3.5: Image produced by $|\mathcal{I}^{KM}(\vec{y}^s, \omega)|$ (see (3.1)) for a waveguide with rigid bottom, depth $D = 200$ m and sound speed $c_0 = 1500$ m/s at frequency $f_0 = 75$ Hz. The scatterer is a square with side $b = 10$ m centered at $(480, 80)$ m. The true boundary of the scatterer is shown in the image with a white square.

As we see from Figure 3.5, the Kirchhoff migration (KM) functional gives a good image of the scatterer, *i.e.*, its location and size are correctly repre-

sented in the image. A classical way to analyze the performance of an imaging method is resolution analysis that is usually performed by computing the point spread function of the imaging functional, *i.e.*, the image obtained for a point scatterer. In the next section, we will perform this analysis for KM in the simplified waveguide environment that we are interested in.

3.2.1 Resolution Analysis

Let us consider a *point* scatterer placed at $\vec{x}^* = (z^*, x^*)$. To simplify the calculations we assume a homogeneous Dirichlet boundary condition on the bottom of the waveguide. For a source placed at $\vec{x}_s = (0, x_s)$ and a receiver placed at $\vec{x}_r = (0, x_r)$ we can approximate the elements of the response matrix for the scattered field by

$$\hat{\Pi}(\vec{x}_r, \vec{x}_s, \omega) = \tau(\omega) \hat{G}(\vec{x}^*, \vec{x}_s, \omega) \hat{G}(\vec{x}_r, \vec{x}^*, \omega). \quad (3.6)$$

Here, we ignored the direct waves going from \vec{x}_s to \vec{x}_r and assumed that the scattered field is simply the Green's function from \vec{x}_s to \vec{x}^* multiplied by the scattering coefficient $\tau(\omega)$ and then by the Green's function from \vec{x}^* to \vec{x}_r . In what follows, we assume that our scatterer is an isotropic point reflector with

$$\tau(\omega) = 1.$$

Using this and replacing the expression for the Green's function given by (2.13) into (3.6), we have

$$\hat{\Pi}(\vec{x}_r, \vec{x}_s, \omega) = -\frac{1}{4} \sum_{m=1}^{\infty} \sum_{n=1}^{\infty} \frac{e^{i\beta_m z^*}}{\beta_m} X_m(x_s) \frac{e^{i\beta_n z^*}}{\beta_n} X_n(x_r) X_m(x^*) X_n(x^*). \quad (3.7)$$

Now, for a $\vec{y}^s = (z^s, x^s)$ in our search domain, the imaging functional (3.1) becomes

$$\begin{aligned} \mathcal{I}^{KM}(\vec{y}^s, \omega) &= \frac{1}{16} \sum_{\vec{x}_s, \vec{x}_r} \sum_{m, n} \sum_{m', n'} \frac{e^{i(\beta_m + \beta_n) z^*}}{\beta_m \beta_n} X_m(x_s) X_n(x_r) X_m(x^*) X_n(x^*) \\ &\quad \times e^{-i(\beta_{m'} + \beta_{n'}) z^s} X_{m'}(x_s) X_{n'}(x_r) X_{m'}(x^s) X_{n'}(x^s). \end{aligned} \quad (3.8)$$

Assuming that the array spans the whole depth of the waveguide with an array pitch h small enough, we can approximate the double sum in (3.8) by a double integral over x_s and x_r , giving us

$$\begin{aligned} \mathcal{I}^{KM}(\bar{y}^s, \omega) &\simeq \frac{1}{16} \frac{1}{h^2} \sum_{m,n,m',n'} \frac{e^{i(\beta_m+\beta_n)z^*}}{\beta_m\beta_n} X_m(x^*)X_n(x^*)e^{-i(\beta_{m'}+\beta_{n'})z^s} X_{m'}(x^s) \\ &\times X_{n'}(x^s) \int_0^D X_m(x_s)X_{m'}(x_s) dx_s \int_0^D X_n(x_r)X_{n'}(x_r) dx_r. \end{aligned} \quad (3.9)$$

Since the eigenfunctions $X_n(x)$ are orthonormal, the only surviving terms in the sum will be those where $m = m'$ and $n = n'$. Hence

$$\mathcal{I}^{KM}(\bar{y}^s, \omega) \simeq \frac{1}{16} \frac{1}{h^2} \sum_{m,n} \frac{e^{i(\beta_m+\beta_n)(z^*-z^s)}}{\beta_m\beta_n} X_m(x^*)X_n(x^*)X_m(x^s)X_n(x^s). \quad (3.10)$$

Cross-range resolution

To examine the resolution in cross-range, we assume that the wavelength λ_0 is much smaller than the depth ($\lambda_0 \ll D$) and that the search point is at $\bar{y}^s = (z^*, x^s)$, i.e. it is located at the correct range $z = z^*$. Assuming also that the point source is located sufficiently far from the source (i.e. $|z^*|$ is large enough), the imaging functional (3.10) simplifies to

$$\mathcal{I}^{KM}(\bar{y}^s, \omega) \simeq \frac{1}{4h^2 D^2} \sum_{m,n=1}^M \frac{1}{\beta_m\beta_n} \sin \frac{m\pi x^*}{D} \sin \frac{n\pi x^*}{D} \sin \frac{m\pi x^s}{D} \sin \frac{n\pi x^s}{D}, \quad (3.11)$$

where only the propagating modes have been taken into account.

We define the quantities $\xi_m = \frac{\lambda_0 m}{2D}$, $\xi_n = \frac{\lambda_0 n}{2D}$ and replace the sum over m, n by an integral over ξ_m and ξ_n ,

$$\begin{aligned}
\mathcal{I}^{KM}(\vec{y}^s, \omega) &\simeq \frac{1}{4\pi^2 h^2} \int_0^1 \frac{1}{\sqrt{1-\xi_m^2}} \sin\left(\frac{\xi_m 2\pi x^*}{\lambda_0}\right) \sin\left(\frac{\xi_m 2\pi x^s}{\lambda_0}\right) d\xi_m \\
&\quad \times \int_0^1 \frac{1}{\sqrt{1-\xi_n^2}} \sin\left(\frac{\xi_n 2\pi x^*}{\lambda_0}\right) \sin\left(\frac{\xi_n 2\pi x^s}{\lambda_0}\right) d\xi_n \\
&= \frac{1}{16\pi^2 h^2} \int_0^1 \frac{1}{\sqrt{1-\xi_m^2}} \left[\cos\left(\frac{2\pi\xi_m}{\lambda_0}(x^* - x^s)\right) - \cos\left(\frac{2\pi\xi_m}{\lambda_0}(x^* + x^s)\right) \right] d\xi_m \\
&\quad \times \int_0^1 \frac{1}{\sqrt{1-\xi_n^2}} \left[\cos\left(\frac{2\pi\xi_n}{\lambda_0}(x^* - x^s)\right) - \cos\left(\frac{2\pi\xi_n}{\lambda_0}(x^* + x^s)\right) \right] d\xi_n.
\end{aligned} \tag{3.12}$$

In Figure 3.6, we show the plot of function (3.12) that determines the cross-range resolution for a waveguide with a soft bottom, depth $D = 200$ m, sound speed $c_0 = 1500$ m/s and frequency $f_0 = 75$ Hz, for fixed $z = z^*$ at the correct range.

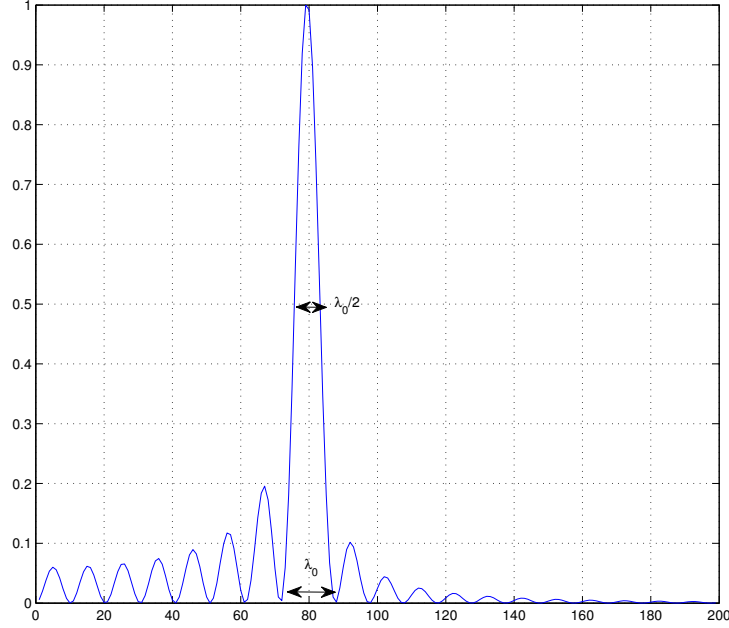


Figure 3.6: Plot of the function (3.12) for $D = 200$ m, $c_0 = 1500$ m/s, $f_0 = 75$ Hz, for a point scatterer placed at $(z^*, x^*) = (480, 80)$ m.

Range resolution

To examine the resolution in range we assume that the search point is located at the correct depth, i.e. at $\vec{y}^s = (z^s, x^*)$. In this case, the expression for the imaging functional is

$$\mathcal{I}^{KM}(\vec{y}^s, \omega) \simeq \frac{1}{4h^2 D^2} \sum_{m,n} \frac{e^{i(\beta_n + \beta_m)(z^* - z^s)}}{\beta_n \beta_m} \sin^2 \left(\frac{m\pi x^*}{D} \right) \sin^2 \left(\frac{n\pi x^*}{D} \right). \quad (3.13)$$

With ξ_m and ξ_n as before, we approximate the sum over m, n by the integral over ξ_m and ξ_n , to get

$$\begin{aligned} \mathcal{I}^{KM}(\vec{y}^s, \omega) &\simeq \frac{1}{4\pi^2 h^2} \int_0^1 \int_0^1 \frac{1}{\sqrt{1 - \xi_m^2} \sqrt{1 - \xi_n^2}} \sin^2 \left(\frac{2\xi_m \pi x^*}{\lambda_0} \right) \sin^2 \left(\frac{2\xi_n \pi x^*}{\lambda_0} \right) \\ &\quad \times \exp \left\{ i \left(\sqrt{\frac{\omega^2}{c_0^2} - \frac{\omega^2}{c_0^2} \xi_m^2} + \sqrt{\frac{\omega^2}{c_0^2} - \frac{\omega^2}{c_0^2} \xi_n^2} \right) (z^* - z^s) \right\} d\xi_m d\xi_n \\ &= \frac{1}{16\pi^2 h^2} \int_0^1 \frac{1}{\sqrt{1 - \xi_m^2}} \left[1 - \cos \left(\frac{4\pi \xi_m x^*}{\lambda_0} \right) \right] e^{\frac{2i\pi}{\lambda_0} \sqrt{1 - \xi_m^2} (z^* - z^s)} d\xi_m \\ &\quad \int_0^1 \frac{1}{\sqrt{1 - \xi_n^2}} \left[1 - \cos \left(\frac{4\pi \xi_n x^*}{\lambda_0} \right) \right] e^{\frac{2i\pi}{\lambda_0} \sqrt{1 - \xi_n^2} (z^* - z^s)} d\xi_n. \end{aligned} \quad (3.14)$$

In Figure 3.7 we show the plot of the modulus of (3.14), that determines the range resolution for a waveguide with a soft bottom, depth $D = 200$ m, sound speed $c_0 = 1500$ m/s and frequency $f_0 = 75$ Hz, for fixed $x = x^*$ at the correct cross-range.

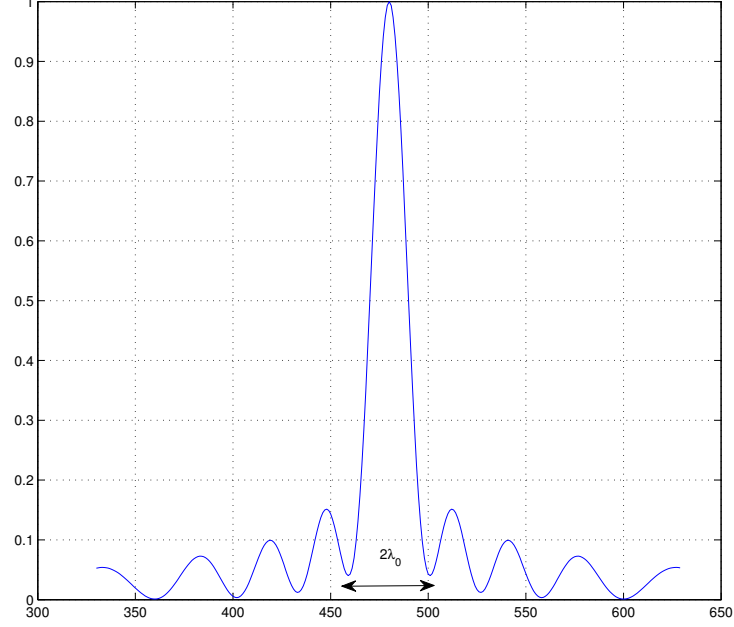


Figure 3.7: Plot of the modulus of function (3.14) for $D = 200$ m, $c_0 = 1500$ m/s, $f_0 = 75$ Hz, for a point scatterer placed at $(z^*, x^*) = (480, 80)$ m .

Remark 1 *The plots in Figures 3.6 and 3.7 show the point spread function (PSF) of KM as a function of cross-range and range respectively. We observe that the PSF is centered at the correct location of the scatterer. The resolution of the imaging method can be determined using these plots. If we define, for example, as the resolution the width of the PSF at half its maximal value we obtain a cross-range resolution of $\lambda_0/2$ (see Figure 3.6). Alternatively, we could measure the width of the PSF at the first zero which gives a cross-range resolution of λ_0 (see Figure 3.6). Any of these values can be used, as long as, we make clear how resolution is defined.*

Remark 2 *For an extended object with constant reflectivity, assuming linearity (i.e., using Born approximation), we can show that the KM image is the convolution of the PSF with the indicator function of the object. More generally, in the linear case, the image we obtain is the convolution of the reflectivity of the scatterer with the PSF. That is why studying the point spread*

function of the imaging method is important in practice.

3.3 Selective Imaging

After successfully creating an image of an extended reflector (see Figure 3.5), our next goal is to image specific parts of it. One way of achieving this, is by using the subspace projection method. The subspace projection method [4], is based on the singular value decomposition (SVD) (see, for example, [9, §2.5]) of the array response matrix. If $\hat{\Pi}(\omega)$ is our $N \times N$ ($N = N_s = N_r$) response matrix in the frequency domain for a fixed frequency, the SVD of $\hat{\Pi}(\omega)$ is a factorization of the form

$$\hat{\Pi}(\omega) = U(\omega)\Sigma(\omega)V^*(\omega),$$

where Σ is a diagonal matrix containing the singular values σ_i of $\hat{\Pi}(\omega)$ in descending order, and U , V are unitary matrices containing the left and right singular vectors, respectively. For the sake of brevity we shall omit the ω 's in the sequel.

The main idea behind the subspace projection method is to create a filtered version of the array response matrix and use it for imaging. If we write the SVD of $\hat{\Pi}(\omega)$ as a sum,

$$\hat{\Pi}(\omega) = \sum_{i=1}^r \sigma_i U_i V_i^*,$$

where $r = \text{rank}(\hat{\Pi}(\omega))$ so that $\sigma_1 \geq \dots \geq \sigma_r > \sigma_{r+1} = \dots = \sigma_N = 0$ and where U_i and V_i are the left and right singular vectors, respectively, we can create a filtered version, by adding what we call the filter weights $d_i \in \{0, 1\}$. In the case where a weight $d_i = 1$, that simply means that we will include the i -th singular vector to create the filtered version of the response matrix, while $d_i = 0$ means that the i -th singular vector will be excluded. So, the filtered version of the response matrix may be written as,

$$D[\hat{\Pi}(\omega)] = \sum_{i=1}^r d_i \sigma_i U_i V_i^*.$$

If we replace the expression for \hat{G}_0 given by (3.3) into (3.1) we get

$$\mathcal{I}^{KM}(\vec{y}^s, \omega) = -\frac{1}{4} \sum_{\vec{x}_s, \vec{x}_r} \hat{\Pi}(\vec{x}_r, \vec{x}_s, \omega) \sum_{m,n} e^{-i(\beta_m + \beta_n)|z - z_s|} \quad (3.15)$$

$$X_m(x_s) X_m(x^s) X_n(x_r) X_n(x^s).$$

Now, replacing the response matrix by its filtered version, we create our image with

$$\mathcal{I}^{KM,f}(\vec{y}^s, \omega) = -\frac{1}{4} \sum_{\vec{x}_s, \vec{x}_r} \left(D[\hat{\Pi}(\omega)] \right)_{rs} \sum_{m,n} e^{-i(\beta_m + \beta_n)|z - z_s|} \quad (3.16)$$

$$X_m(x_s) X_m(x^s) X_n(x_r) X_n(x^s).$$

Again, if we have multi-frequency data, we can compute instead,

$$\mathcal{I}^{KM,f}(\vec{y}^s) = \left| \sum_{\omega} \mathcal{I}^{KM,f}(\vec{y}^s, \omega) \right|. \quad (3.17)$$

Let us also define

$$\mathcal{I}_J^{KM}(\vec{y}^s, \omega) = -\frac{1}{4} \sum_{\vec{x}_s, \vec{x}_r} \sigma_J(\omega) U_J(\omega) V_J^*(\omega) \sum_{m,n} e^{-i(\beta_m + \beta_n)|z - z_s|} \quad (3.18)$$

$$X_m(x_s) X_m(x^s) X_n(x_r) X_n(x^s),$$

and

$$\mathcal{I}_J^{KM}(\vec{y}^s) = \left| \sum_{\omega} \mathcal{I}_J^{KM}(\vec{y}^s, \omega) \right|, \quad (3.19)$$

the KM functional obtained with one or many frequencies when only the projection on the J -th singular vector of the response matrix is used.

3.4 Modal Projection and selective imaging

In the case where our array spans the whole depth of the waveguide with an array pitch h small enough, we can replace the double sum in (3.15) by a

double integral over \vec{x}_s and \vec{x}_r , giving us

$$\begin{aligned}
\mathcal{I}^{KM}(\vec{y}^s, \omega) &= -\frac{1}{4h^2} \int_0^D \int_0^D \hat{\Pi}(\vec{x}_s, \vec{x}_r, \omega) \sum_{m,n} e^{-i(\beta_n + \beta_m)|z_a - z^s|} \\
&\quad X_m(x_s) X_m(x^s) X_n(x_r) X_n(x^s) dx_r dx_s \\
&= -\frac{1}{4h^2} \sum_{m,n} e^{-i(\beta_n + \beta_m)|z_a - z^s|} X_m(x^s) X_n(x^s) \\
&\quad \int_0^D \int_0^D \hat{\Pi}(\vec{x}_s, \vec{x}_r, \omega) X_m(x_s) X_n(x_r) dx_r dx_s. \tag{3.20}
\end{aligned}$$

Now, let us introduce a matrix $\hat{\mathbb{P}}(\omega)$, such that for all $m, n = 1, 2, \dots, M$,

$$\hat{\mathbb{P}}_{mn}(\omega) = \beta_n \beta_m \int_0^D \int_0^D \hat{\Pi}(\vec{x}_s, \vec{x}_r, \omega) X_m(x_s) X_n(x_r) dx_r dx_s. \tag{3.21}$$

In (3.21) we multiply the double integral by $\beta_m \beta_n$ to eliminate the $\beta_m \beta_n$ that appear in the denominator of $\hat{\Pi}$ (see for example (3.7)). This is not just the modal projection of the response matrix, and the reasoning behind this normalization will be explained in Chapter 5.

Now, using (3.21) in (3.20) gives

$$\mathcal{I}^{KM}(\vec{y}^s, \omega) = -\frac{1}{4h^2} \sum_{m,n} \frac{e^{-i(\beta_n + \beta_m)|z_a - z^s|}}{\beta_n \beta_m} X_n(x^s) X_m(x^s) \hat{\mathbb{P}}_{mn}(\omega). \tag{3.22}$$

Instead of using (3.22) we propose to use the following imaging functional

$$\tilde{\mathcal{I}}^{KM}(\vec{y}^s, \omega) = -\frac{1}{4} \sum_{m,n} e^{-i(\beta_n + \beta_m)|z_a - z^s|} X_n(x^s) X_m(x^s) \hat{\mathbb{P}}_{mn}(\omega). \tag{3.23}$$

Again, it might not be clear why we chose to omit the $\beta_m \beta_n$ in (3.22). We will explain the reason behind this choice in Chapter 5.

When we want to use selective imaging, we create our image in the same way as before, using the filtered version of $\hat{\mathbb{P}}$,

$$\tilde{\mathcal{I}}^{KM,f}(\vec{y}^s, \omega) = -\frac{1}{4} \sum_{m,n} e^{-i(\beta_n + \beta_m)|z_a - z^s|} X_n(y^s) X_m(y^s) \left(D[\hat{\mathbb{P}}(\omega)] \right)_{mn}, \tag{3.24}$$

and for multi-frequency data, we compute,

$$\tilde{\mathcal{I}}^{KM,f}(\vec{y}^s) = \left| \sum_{\omega} \tilde{\mathcal{I}}^{KM,f}(\vec{y}^s, \omega) \right|. \quad (3.25)$$

The only thing that changes in the process is the size of the response matrix. Now, we are dealing with an $M \times M$ matrix, with M denoting the number of propagating modes.

As for KM we can define

$$\tilde{\mathcal{I}}_J^{KM}(\vec{y}^s, \omega) = -\frac{1}{4} \sum_{m,n} e^{-i(\beta_n + \beta_m)|z_a - z^s|} X_n(y^s) X_m(y^s) (\sigma_J(\omega) U_J(\omega) V_J^*(\omega))_{mn}, \quad (3.26)$$

and

$$\tilde{\mathcal{I}}_J^{KM}(\vec{y}^s) = \left| \sum_{\omega} \tilde{\mathcal{I}}_J^{KM}(\vec{y}^s, \omega) \right|, \quad (3.27)$$

where by abusing slightly, the notation we have used $\sigma_J(\omega) U_J(\omega) V_J^*(\omega)$ to denote the projection on the J -th singular vector of $\hat{\mathbb{P}}(\omega)$.

Chapter 4

Numerical Simulations

As mentioned in Section 2.2.1, we must use a numerical method to compute the solution of the initial/boundary value problem for the total field. To this end, we have used Montjoie [1], a high-order finite element C++ code developed by Marc Durufle, designed to solve equations that arise in wave propagation problems. In particular, Montjoie can deal with acoustic, electromagnetic, aeroacoustic and elastodynamic problems.

4.1 Description of the numerical method

In order to be able to solve (2.3) numerically with a mixed, spectral finite element method, we have to make some approximations.

First, we approximate the Dirac pulse as a source term by a function $f(t, \vec{x}) = h(t)g(\vec{x}; \vec{x}_s)$. Here $h(t)$ is a Ricker function in time, given by

$$h(t) = (1 - f_0\sqrt{2}(t - t_c))e^{-(f_0\pi\sqrt{2}(t-t_c))^2},$$

where f_0 is the central frequency of the pulse and t_c is the time at which the source attains its maximum. The function $g(\vec{x}; \vec{x}_s)$ is a Gaussian, given by

$$g(\vec{x}; \vec{x}_s) = \beta e^{(-\alpha|\vec{x}-\vec{x}_s|^2)},$$

where $\alpha = \ln(10^6)/r^2$, r is the radius of the Gaussian and $\beta = \sqrt{2\pi/\alpha}$.

Secondly, in order to use a finite element method, we have to truncate our original infinite domain into a bounded computational domain. We want

to simulate wave propagation in an unbounded domain in z , so in order to do this, we introduce perfectly matched layers (see [2, 8]), on the left and right sides of our truncated domain.

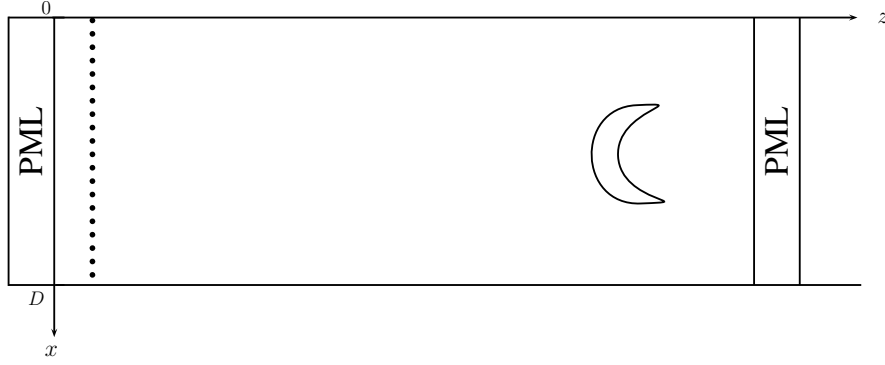


Figure 4.1: Schematic representation of a waveguide truncated near and far from the source with two perfectly matched layers.

A perfectly matched layer is a layer of artificial absorbing material that is placed adjacent to the lateral edges of the grid. When a wave enters the absorbing layer, it is attenuated and decays exponentially inside the layer; even if it reflects off the boundary at the end of the layer, the returning wave after one round trip through the absorbing layer is exponentially small.

After making these approximations, we can begin to describe the numerical method we used to solve the problem. To solve the problem in space, we use a finite element method. We discretize our domain with squares. On these squares, we define polynomials of the Q_n family, where $Q_n = \text{span}\{x^l y^m, 0 \leq l, m \leq n\}$ and use Gauss-Lobatto points $\xi_{lm} = (\cos \frac{\pi l}{n}, \cos \frac{\pi m}{n})$ for the numerical integration (see Figure ?? for $n = 4$).

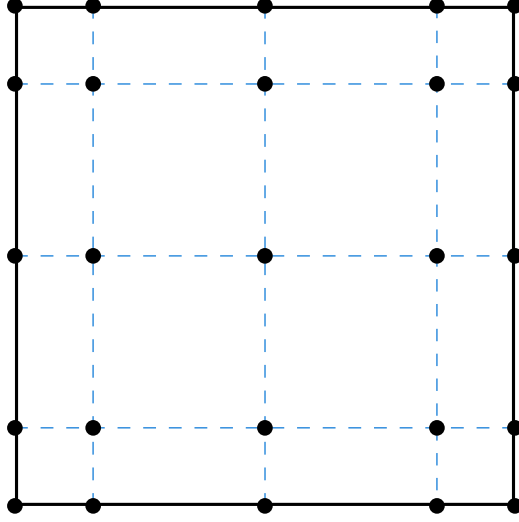


Figure 4.2: An example of G-L points, for $n = 4$.

In order to compute the solution in time, we first define a final computation time T . We then discretize our time window uniformly and use a n -th order leapfrog scheme to compute the solution.

4.2 Implementation

After describing the basic principles of our numerical method, we can talk about the specifics of the problem and the numerical method. First, let us give some details about the problem. The waveguide, as described in Section 2.1, is of depth $D = 200$ m and we have a vertical array, placed at $z_a = 40$ m, consisting of 39 transducers spread uniformly across the array with a pitch of $h = 5$ m. The results we will present in the next section pertain to acoustically hard and square shaped scatterers with side lengths $b = 10$ m and $b = 40$ m, centered at $(z, x) = (480, 100)$ m.

Our computational domain in space is the rectangle $(z, x) \in [0, 500] \times [0, 200]$ that we discretized using squares with side 10 m. In each square we used Q_8 polynomials. The time interval in which the solution was computed is $t \in [0, 4]$ s, discretized with a time step of $\Delta t = 2.5 \cdot 10^{-5}$ s. For the time-discretization we used a 4th order leapfrog scheme.

The source used has a central frequency of $f_0 = 75$ Hz, which corresponds

to a wavelength of $\lambda_0 = 20$ m and $M = 20$ propagating modes.

4.3 Numerical Results

In this section, we will present imaging results that were produced with a pulse, with a central frequency $f_0 = 75$ Hz and a bandwidth of $B = 10$ Hz, so we work with frequencies $f \in [70, 80]$ Hz, with a discretization step of 0.25 Hz. We will show results for two scatterers with side lengths $b = 5$ ($= \lambda_0/2$) m and $b = 40$ ($= 2\lambda_0$) m, respectively, in a waveguide with a soft bottom.

Object with side length $b = \lambda_0/2$.

First, let us look at the data we used to create the images. In Figure 4.3, we show the traces, as they were recorded at the receivers as a function of time, for the central source of the array, placed at $\vec{x}_s = (40, 100)$ m and when we have the scatterer with side $\lambda_0/2$ in the medium.

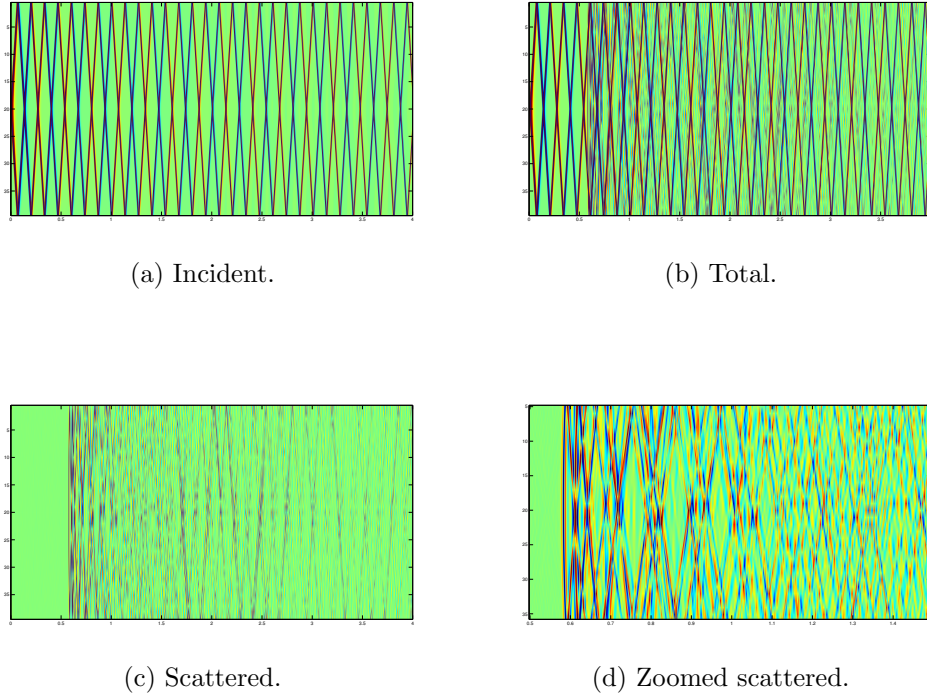


Figure 4.3: Traces for an object with side $\lambda/2$.

We observe that the traces for the incident and total field coincide in the beginning, until the reflections from our scatterer arrive. That also explains the lack of any signal for the same time for the traces corresponding to the scattered field.

In Figure 4.4 we show the image produced by the Kirchhoff migration functional (3.4).

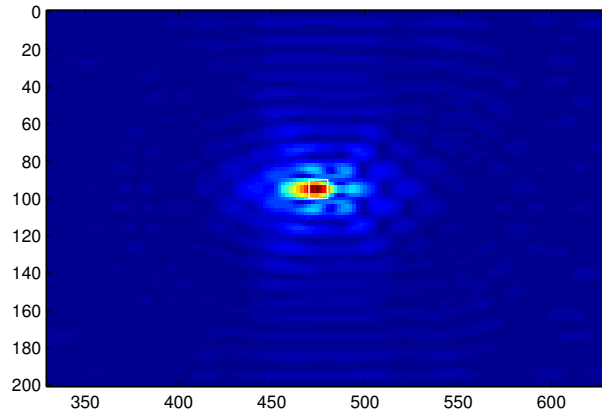


Figure 4.4: Image produced by \mathcal{I}^{KM} (3.4), $b = 10$ m, $D = 200$ m, $c_0 = 1500$ m/s, $f_0 = 75$ Hz, $B = 10$ Hz.

In Figures 4.5 and 4.6, we show images created after using selective imaging for both the response matrix $\hat{\Pi}(\omega)$ and the matrix $\hat{\mathbb{P}}(\omega)$ that we obtain after the projection of the response matrix on the propagating modes. On the following figures, J denotes that we used the J -th singular vector in order to create a filtered version of the response matrix. On the left column we show images created by using selective imaging and \mathcal{I}_J^{KM} (3.19), while on the right we used $\tilde{\mathcal{I}}_J^{KM}$ (3.27).

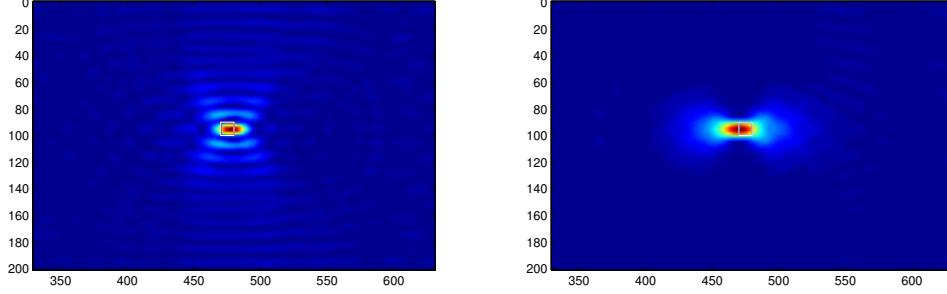


Figure 4.5: Image produced by \mathcal{I}_J^{KM} (left) and $\tilde{\mathcal{I}}_J^{KM}$ (right), $b = 10$ m, $D = 200$ m, $c_0 = 1500$ m/s, $f_0 = 75$ Hz, $J = 1$.

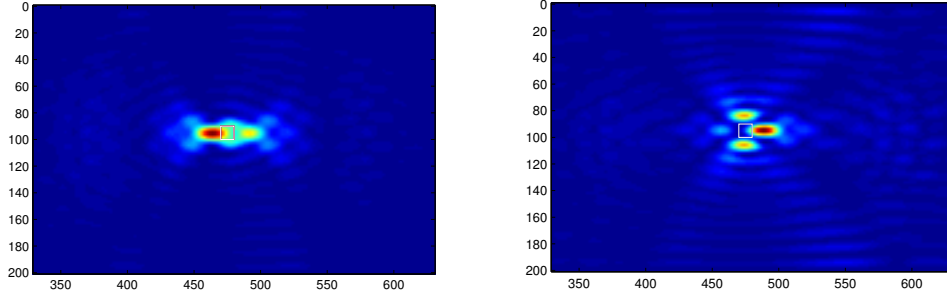
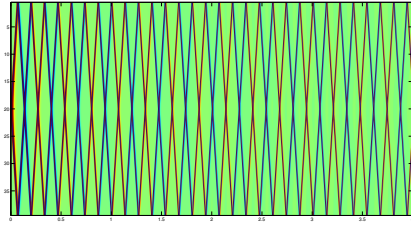


Figure 4.6: Image produced by \mathcal{I}_J^{KM} (left) and $\tilde{\mathcal{I}}_J^{KM}$ (right), $b = 10$ m, $D = 200$ m, $c_0 = 1500$ m/s, $f_0 = 75$ Hz, $J = 2$.

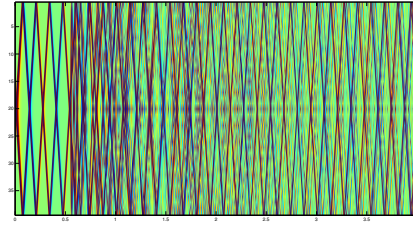
We see that when projecting on the first singular vector, the image appears to be close to the image we showed in 4.4, that we have obtained by using the whole matrix. Also, the projection on the second singular vector seems to miss the object. This intuitively indicates that the first singular vector carries most of the information for this object, while the second singular vector has little information about it. We will try to explore this further and justify this behavior in the next chapter.

Object with side length $b = 2\lambda_0$.

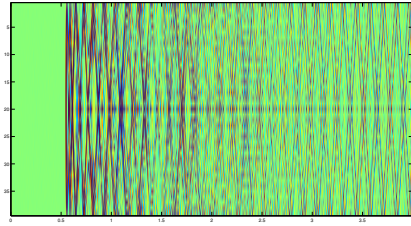
Now, let us increase the size of the scatterer to $b = 2\lambda_0 = 40$ m. As we see in Figure 4.7, the reflections from the scatterer now are much stronger, thus creating a much more complicated signal on the total field.



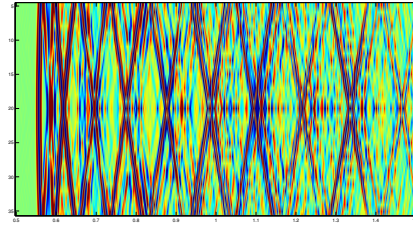
(a) Incident.



(b) Total.



(c) Scattered.



(d) Zoomed scattered.

Figure 4.7: Traces for an object with side 2λ .

In Figure 4.8, we see the image created for the current object by using the Kirchhoff migration functional (3.4).

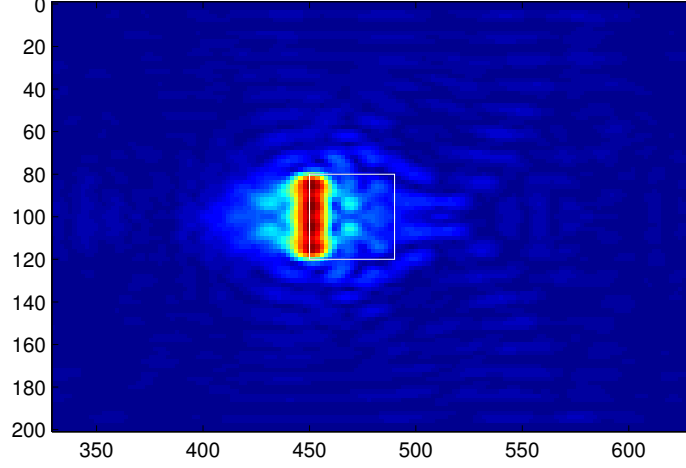
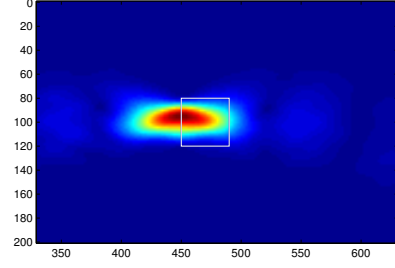
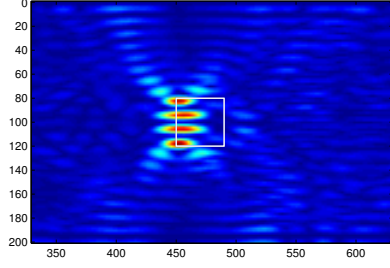


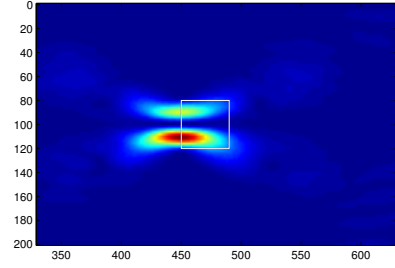
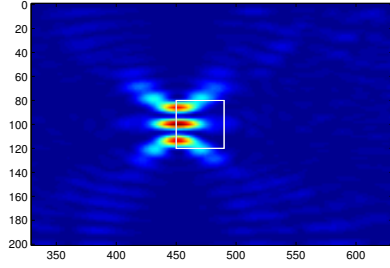
Figure 4.8: Image produced by \mathcal{I}^{KM} , $b = 40$ m, $D = 200$ m, $c_0 = 1500$ m/s, $f_0 = 75$ Hz, $B = 10$ Hz.

We notice that only the left side of the object is recreated. This can be explained intuitively; since the array is on the left side of the object, only the rays that are reflected on the left side of the square scatterer travel back to the receivers, therefore we only have data concerning the left side.

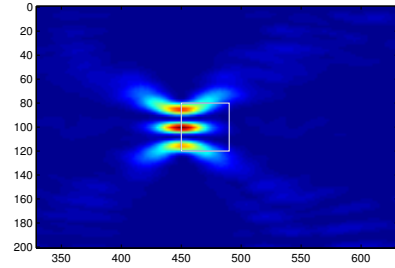
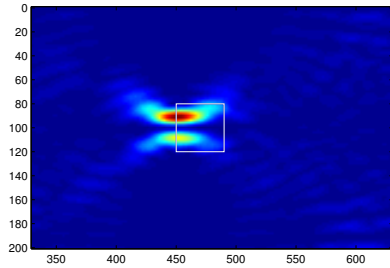
Again, in Figure 4.9, the figures on the left column correspond to images created by using selective imaging and \mathcal{I}_J^{KM} , while on the right we used $\tilde{\mathcal{I}}_J^{KM}$ and J denotes that we used the J -th singular vector.



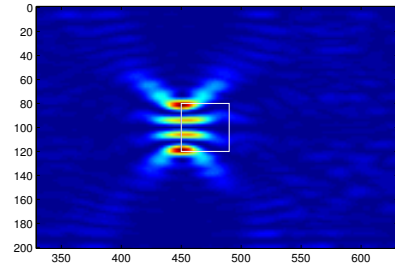
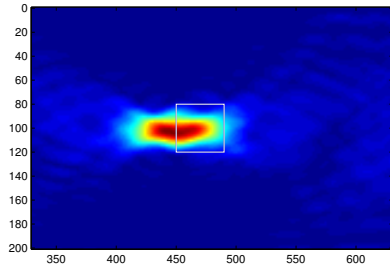
J=1



J=2



J=3



J=4

Figure 4.9: Values of \mathcal{I}_J^{KM} (left) and $\tilde{\mathcal{I}}_J^{KM}$ (right), for $b = 40$ m, $D = 200$ m, $c_0 = 1500$ m/s, $f_0 = 75$ Hz, $B = 10$ Hz. J denotes the projection on the J -th singular vector.

In the case of the larger object, we can observe the results of selective imaging much better. We see that when we use \mathcal{I}_J^{KM} the first singular vector seems to be focusing towards the edges of the object, while as we use the next singular vectors, the image seems to be shifting its focus towards the middle of the object. However, when using $\tilde{\mathcal{I}}_J^{KM}$, we see the opposite behavior, meaning that the first singular vector seems to be focusing toward the middle of the object, while as we use the next singular vectors, the image seems to be shifting its focus towards the edges of the object. We will investigate further and try to explain this behavior in the next chapter.

Chapter 5

Analysis of the imaging method

In the present chapter we will consider and analyze a simplified model problem which will allow us to obtain some explicit expressions of the array response matrix which, in turn, will help us to investigate and understand the phenomena we have observed in the selective imaging approach of the previous chapter.

Specifically, we consider the following model problem: Our waveguide is a uniform strip of depth D . The surface of the waveguide lies along the horizontal z axis, and the bottom is assumed to be acoustically soft. At the origin, there is an active vertical array, which spans the whole depth of the waveguide, with N transducers whose coordinates are $(0, x_i)$, $1 \leq i \leq N$. Each transducer that sends out a signal is viewed as a point source. The target, denoted by \mathcal{T} , is assumed to be a vertical one-dimensional perfect reflector, *i.e.* a ‘crack’ of width b located at range $z = L$. The middle point of the target is denoted by $\vec{y}^* = (L, x_0)$. Let us also denote by \mathcal{I} the vertical section of the waveguide at range $z = L$, *i.e.* $\mathcal{I} := \{(L, x) : 0 \leq x \leq D\}$. This setup is schematically depicted in Figure 5.1 and aims at simulating the left side of the square scatterer which we have examined in the previous chapter. For an analogous setup used to analyze the response matrix for extended targets in the free space we refer to [21].

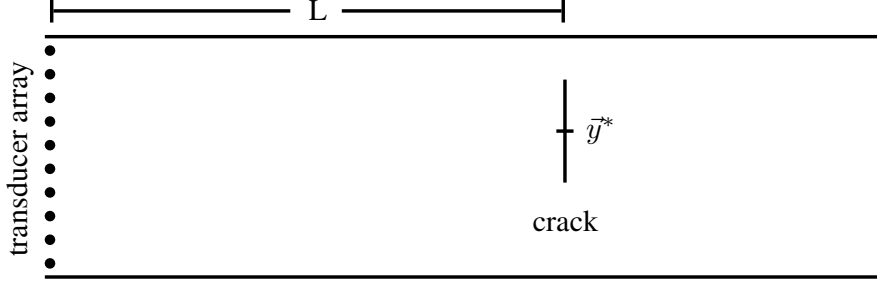


Figure 5.1: A vertical crack, implemented in the waveguide.

5.1 Array response matrix

Assuming a unit reflectivity at each point of the target we may approximate the response in a receiver placed at $\vec{x}_r = (0, x_r)$ due to a source at $\vec{x}_s = (0, x_s)$, $r, s \in \{1, 2, \dots, N\}$, as

$$\hat{\Pi}(\vec{x}_r; \vec{x}_s, \omega) = \int_{\mathcal{T}} \hat{G}(\vec{y}, \vec{x}_r) \hat{G}(\vec{y}, \vec{x}_s) dx, \quad (5.1)$$

where $\vec{y} = (L, x)$, $x \in [x_0 - b/2, x_0 + b/2]$, and \hat{G} is the Green's function as it appears in (2.13). For future reference, let us also recall that $\lambda_n = (n\pi/D)^2$, $X_n(x) = \sqrt{2/D} \sin(\sqrt{\lambda_n}x)$, $n = 1, 2, \dots$, denote the eigenvalues and corresponding eigenfunctions of the two-point vertical eigenvalue problem $X''(x) + \lambda X(x) = 0$, $X(0) = X(D) = 0$, and the coefficients β_n in (2.13) are defined in (2.12).

Inserting (2.13) into (5.1) shows that

$$\hat{\Pi}(\vec{x}_r; \vec{x}_s, \omega) = -\frac{1}{4} \sum_{m,n=1}^{\infty} \frac{e^{i\beta_m L}}{\beta_m} X_m(x_s) X_n(x_r) \frac{e^{i\beta_n L}}{\beta_n} \int_{x_0 - \frac{b}{2}}^{x_0 + \frac{b}{2}} X_m(x) X_n(x) dx. \quad (5.2)$$

Moreover, let $g_m(x_i) := \frac{i}{2} \frac{e^{i\beta_m L}}{\beta_m} X_m(x_i) = \left(\hat{G}(\cdot, \vec{x}_i), X_m \right)_{L^2(\mathcal{I})}$, where the outer parentheses in the second equality denote the standard L^2 inner product

on \mathcal{I} . Let us also define \mathcal{G} to be the matrix

$$\mathcal{G} := \begin{pmatrix} g_1(x_1) & g_2(x_1) & \dots & g_M(x_1) & g_{M+1}(x_1) & \dots \\ g_1(x_2) & g_2(x_2) & \dots & g_M(x_2) & g_{M+1}(x_2) & \dots \\ \vdots & \vdots & & \vdots & \vdots & \\ g_1(x_N) & g_2(x_N) & \dots & g_M(x_N) & g_{M+1}(x_N) & \dots \end{pmatrix}$$

and A the (infinite) matrix with entries

$$A_{mn} = \int_{x_0 - \frac{b}{2}}^{x_0 + \frac{b}{2}} X_m(x) X_n(x) dx, \quad m, n = 1, 2, \dots \quad (5.3)$$

Then, using (5.2), we may write the array response matrix $\hat{\Pi}$ as a matrix product of the form

$$\hat{\Pi} = \mathcal{G} A \mathcal{G}^T. \quad (5.4)$$

We point out that if L is sufficiently large and if $m \geq M + 1$, then

$$g_m(x_i) = \frac{i}{2} \frac{e^{i\beta_m L}}{\beta_m} X_m(x_i) = \frac{1}{2} \frac{e^{-\sqrt{\lambda_n - k^2} L}}{\sqrt{\lambda_n - k^2}} X_m(x_i) \simeq 0,$$

or, in other words, only the principal $N \times M$ part of \mathcal{G} is practically non-zero. Note also, that if $h = D/(N + 1)$ is the distance between any two consecutive transducers, then for N sufficiently large, the orthonormality of the eigenfunctions infers

$$\begin{aligned} (\mathcal{G}^T \mathcal{G})_{mn} &= \sum_{k=1}^N g_m(x_k) g_n(x_k) = -\frac{1}{4} \sum_{k=1}^N \frac{e^{i(\beta_m + \beta_n)L}}{\beta_m \beta_n} X_m(x_k) X_n(x_k) \\ &= -\frac{1}{4} \frac{e^{i(\beta_m + \beta_n)L}}{\beta_m \beta_n} \sum_{k=1}^N X_m(x_k) X_n(x_k) \\ &\simeq -\frac{e^{i(\beta_m + \beta_n)L}}{4\beta_m \beta_n} \frac{1}{h} \int_0^D X_m(x) X_n(x) dx \\ &= -\frac{1}{h} \frac{e^{i(\beta_m + \beta_n)L}}{4\beta_m \beta_n} \delta_{mn}. \end{aligned} \quad (5.5)$$

Hence, $\mathcal{G}^T \mathcal{G}$ is “almost” diagonal, *i.e.* $\mathcal{G}^T \mathcal{G} = \mathcal{D}$, where

$$\mathcal{D}_{mn} = \begin{cases} -\frac{1}{h} \frac{e^{i(\beta_m + \beta_n)L}}{4\beta_m \beta_n}, & m = n \\ 0, & m \neq n. \end{cases} \quad (5.6)$$

Therefore (5.4) and (5.5) imply

$$A = \mathcal{D}^{-1} \mathcal{G}^T \hat{\Pi} \mathcal{G} \mathcal{D}^{-1}. \quad (5.7)$$

Next, it is natural to ask what is the relation between the matrix $\hat{\mathbb{P}}$, which results when we project the array response matrix $\hat{\Pi}$ on the propagating modes and the matrix A . Recall that $\hat{\mathbb{P}}$ is given by the formula

$$\hat{\mathbb{P}}_{mn}(\omega) = \beta_n \beta_m \int_0^D \int_0^D \hat{\Pi}(\vec{x}_r, \vec{x}_s, \omega) X_n(x_s) X_m(x_r) dx_r dx_s,$$

where $m, n = 1, \dots, M$, and M is the number of propagating modes. Then, in view of (5.2) and the orthonormality of the eigenfunctions $\{X_n\}_{n=1,2,\dots}$, it is immediate to see that

$$\hat{\mathbb{P}}_{mn} = -\frac{1}{4} e^{i(\beta_m + \beta_n)L} A_{mn}, \quad m, n = 1, \dots, M. \quad (5.8)$$

Therefore, the $M \times M$ matrix $\hat{\mathbb{P}}$ is related with the $M \times M$ principal part of A , denoted again by A , as

$$\hat{\mathbb{P}} = -\frac{1}{4} Q A Q, \quad (5.9)$$

where Q is the diagonal matrix $\text{diag}(e^{i\beta_1 L}, \dots, e^{i\beta_M L})$ and $Q^* Q = I$, hence $\hat{\mathbb{P}}$ is unitarily equivalent to A .

Now, since we have seen that both matrices $\hat{\Pi}$, $\hat{\mathbb{P}}$, which are involved in the computation of \mathcal{I}^{KM} and $\tilde{\mathcal{I}}^{KM}$, respectively, are related to A , it seems reasonable to turn our attention to the spectral properties of the matrix A , which is obviously a real, symmetric matrix.

For $m, n = 1, 2, \dots, \infty$ and in view of the simple trigonometric identity $2 \sin a \sin b = \cos(a - b) - \cos(a + b)$, we get

$$\begin{aligned} A_{mn} &= \int_{x_0 - \frac{b}{2}}^{x_0 + \frac{b}{2}} X_m(x) X_n(x) dx = \frac{2}{D} \int_{x_0 - \frac{b}{2}}^{x_0 + \frac{b}{2}} \sin \frac{m\pi x}{D} \sin \frac{n\pi x}{D} dx \\ &= \frac{1}{D} \int_{x_0 - \frac{b}{2}}^{x_0 + \frac{b}{2}} \cos \frac{(m-n)\pi x}{D} dx - \frac{1}{D} \int_{x_0 - \frac{b}{2}}^{x_0 + \frac{b}{2}} \cos \frac{(m+n)\pi x}{D} dx. \end{aligned}$$

Hence, A may be viewed as the difference of two matrices T and H , *i.e.* $A = T - H$, where

$$T_{mn} = \frac{1}{D} \int_{x_0 - \frac{b}{2}}^{x_0 + \frac{b}{2}} \cos \frac{(m-n)\pi x}{D} dx \quad \text{and} \quad H_{mn} = \frac{1}{D} \int_{x_0 - \frac{b}{2}}^{x_0 + \frac{b}{2}} \cos \frac{(m+n)\pi x}{D} dx,$$

respectively. We can immediately recognize T as a Toeplitz matrix, *i.e.* a matrix in which its entries are constant along the diagonals, and H as a Hankel matrix, *i.e.* a matrix with constant skew-diagonals (these are the diagonals which are perpendicular to the main diagonal).

There is an extended literature on the spectral properties of Toeplitz or Hankel matrices, indicatively we refer to the book by Grenander and Szegő [11], the review report [10], and the references therein. Nevertheless, perhaps the most relevant work to our setting is the one by Fasino [7], where he studies the spectral properties of Toeplitz-plus-Hankel matrices and shows that these are essentially determined by those of the Toeplitz part. Next, following Fasino's notation with appropriate modifications where needed, we investigate the properties of the matrix A .

Let $\phi(x) \in L^\infty[-D, D]$ be a real function and

$$\phi(x) = \phi_0 + 2 \sum_{k=1}^{\infty} \phi_k \cos(kx), \quad (5.10)$$

be its Fourier cosine series, where

$$\phi_k = \frac{1}{D} \int_0^D \phi(x) \cos(kx) dx. \quad (5.11)$$

For any fixed integer n , we associate the Fourier coefficients of ϕ with the following matrices:

$$T_\phi = [\phi_{i-j}], \quad H_\phi = [\phi_{i+j}], \quad X_\phi = T_\phi - H_\phi, \quad i, j = 0, \dots, n.$$

The function ϕ is referred to as the *generating function* of the matrices T_ϕ , H_ϕ and X_ϕ .

Now, let us denote by $\mathbb{1}_S(x)$ the indicator function of a set S , *i.e.*

$$\mathbb{1}_S(x) = \begin{cases} 1, & x \in S \\ 0, & x \notin S, \end{cases}$$

and define

$$\phi(x) := \mathbb{1}_{[x_0 - \frac{b}{2}, x_0 + \frac{b}{2}]} + \mathbb{1}_{[-x_0 - \frac{b}{2}, -x_0 + \frac{b}{2}]}, \text{ for } x \in [-D, D]. \quad (5.12)$$

Then the Fourier coefficients (5.11) are

$$\phi_k = \frac{1}{D} \int_0^D \phi(x) \cos \frac{(m-n)\pi x}{D} dx = \frac{1}{D} \int_{x_0 - \frac{b}{2}}^{x_0 + \frac{b}{2}} \cos \left(\frac{k\pi x}{D} \right) dx.$$

Therefore, $T_{mn} = \phi_{m-n}$ and $H_{mn} = \phi_{m+n}$.

The asymptotic distribution of the eigenvalues of the Toeplitz matrix T is given by the following theorem due to Grenander and Szegő [11]:

Theorem 1 *If $\lambda_0 \leq \lambda_1 \leq \dots \leq \lambda_n$ are the eigenvalues of T_ϕ and*

$$m = \inf_{-D \leq x \leq D} \phi(x), \quad M = \sup_{-D \leq x \leq D} \phi(x),$$

then $m \leq \lambda_k \leq M$, $k = 0, \dots, n$ and, for any fixed integer k ,

$$\lambda_k \rightarrow m, \quad \lambda_{n-k} \rightarrow M, \quad \text{as } n \rightarrow \infty.$$

Moreover, for every function $g \in C[m, M]$ it holds:

$$\lim_{n \rightarrow \infty} \frac{1}{n+1} \sum_{k=0}^n g(\lambda_k) = \frac{1}{2D} \int_{-D}^D g(\phi(x)) dx.$$

Furthermore, the next theorem by Fasino [7], shows that the spectral properties of infinite matrices of the form $T_f + H_g$ are driven by the Toeplitz part of the matrix.

Theorem 2 *The eigenvalues of the sequences of matrices $T_f + H_g$ and T_f , where f, g are bounded, have the same asymptotic distribution function.*

In our case, for the function ϕ defined in (5.12), Theorem 1 guarantees that the extreme values for the eigenvalues ν_n of the Toeplitz matrix T are

$$m = \inf_{-D \leq x \leq D} \phi(x) = 0 \quad \text{and} \quad M = \sup_{-D \leq x \leq D} \phi(x) = 1.$$

Moreover, considering the function g to be the identity on $[-D, D]$, it holds that

$$\lim_{n \rightarrow \infty} \frac{1}{n+1} \sum_{k=1}^n \nu_k = \frac{1}{2D} \int_{-D}^D \phi(x) dx = \frac{b}{D}.$$

The value b/D indicates the ratio of the non-zero singular values to the total number of singular values. Then, since only the principal $M \times M$ part of the matrix A will play a role in the computation of the array response matrix, where M is the number of propagating modes, which in our case is given by

$$M = \left\lfloor \frac{2D}{\lambda} \right\rfloor,$$

then it is expected that the number of ‘significant’ singular values for our matrix is

$$\left\lceil M \frac{b}{D} \right\rceil = \left\lceil \frac{2b}{\lambda} \right\rceil.$$

We have shown, that the (infinite) matrix A has singular values that are either 0 or 1 and the number of non-zero singular values is related to the size of the object. If we consider that the resolution in cross-range is $\lambda/2$ (see Figure 3.6), then the rank of the matrix (*i.e.*, the number of non-zero singular values) is the size of the object divided by the ‘array resolution’. This has been proven for the case of free space (see [4, §4.5.2]), but, to the best of our knowledge, it is a new result concerning a waveguide geometry.

In the next section we will explore the form of the singular vectors of A , in order to gain some insight into the properties of selective imaging.

5.2 Selective imaging

Let us consider an orthonormal basis $\{Y_j(x)\}_{j=1}^{\infty}$ of $L^2[x_0 - b/2, x_0 + b/2]$. Then, the restriction of the eigenfunctions $X_n \in L^2[0, D]$ on the crack \mathcal{T} may be written as

$$X_n(x)|_{[x_0-b/2, x_0+b/2]} = \sum_{j=1}^{\infty} a_j^n Y_j(x),$$

where

$$a_j^n = \int_{x_0-\frac{b}{2}}^{x_0+\frac{b}{2}} X_n(x) Y_j(x) \, dx.$$

The orthonormality of the Y_i 's implies that

$$A_{mn} = \int_{\mathcal{T}} X_m(x) X_n(x) dx = \int_{\mathcal{T}} \sum_j a_j^m Y_j(x) \sum_i a_i^n Y_i(x) dx = \sum_{i=1}^{\infty} a_i^m a_i^n. \quad (5.13)$$

Let us write

$$\vec{a}_i = (a_i^1, a_i^2, \dots, a_i^M, \dots)^T. \quad (5.14)$$

Then the matrix A may be written as

$$A = \sum_{i=1}^{\infty} \vec{a}_i \vec{a}_i^T. \quad (5.15)$$

Now, we are going to check whether the \vec{a}_i are orthogonal. If this holds, then (5.15) may be viewed as the SVD of A , where all the singular values are equal to 1. Indeed,

$$\begin{aligned} \vec{a}_i \cdot \vec{a}_j &= \sum_{n=1}^{\infty} a_i^n a_j^n = \sum_n \int_{x_0 - \frac{b}{2}}^{x_0 + \frac{b}{2}} X_n(x) Y_i(x) dx \int_{x_0 - \frac{b}{2}}^{x_0 + \frac{b}{2}} X_n(x') Y_j(x') dx' \\ &= \int_{\mathcal{T}} \int_{\mathcal{T}} Y_i(x) Y_j(x') \sum_{n=1}^{\infty} X_n(x) X_n(x') dx dx'. \end{aligned} \quad (5.16)$$

The orthonormality of X_n , $n = 1, 2, \dots$, allows us to write down the following formal eigenfunction expansion of the delta function

$$\delta(x - x') = \sum_{n=1}^{\infty} X_n(x) X_n(x'). \quad (5.17)$$

Therefore (5.16) and (5.17) imply that

$$\begin{aligned} \vec{a}_i \cdot \vec{a}_j &= \int_{x_0 - \frac{b}{2}}^{x_0 + \frac{b}{2}} \int_{x_0 - \frac{b}{2}}^{x_0 + \frac{b}{2}} \delta(x - x') Y_i(x) Y_j(x') dx dx' \\ &= \int_{x_0 - \frac{b}{2}}^{x_0 + \frac{b}{2}} Y_i(x) Y_j(x) dx = \delta_{ij}. \end{aligned}$$

Now we are in a position to write down an expression for the imaging functional $\tilde{\mathcal{I}}_J^{KM}$, where the subscript J is used to indicate that we want to

use selective imaging in the sense that the matrix $\hat{\mathbb{P}}$ will be approximated by means of the J -th singular vector. Specifically, for a search point $\vec{y}^s = (L, x^s)$ located at the correct range L , (3.23), (5.8) and (5.13) imply that

$$\begin{aligned}\tilde{\mathcal{I}}_J^{KM}(\vec{y}^s) &= \sum_{m,n} X_m(x^s) X_n(x^s) a_J^m a_J^n \\ &= \left(\sum_n X_n(x^s) a_J^n \right) \left(\sum_m X_m(x^s) a_J^m \right) \\ &= \left(\sum_n X_n(x^s) a_J^n \right)^2.\end{aligned}$$

So,

$$\begin{aligned}\sqrt{\tilde{\mathcal{I}}_J^{KM}(\vec{y}^s)} &= \left| \sum_n X_n(x^s) a_J^n \right| \\ &= \left| \sum_n X_n(x^s) \int_{x_0 - \frac{b}{2}}^{x_0 + \frac{b}{2}} X_n(x) Y_J(x) dx \right| \\ &= \left| \int_{x_0 - \frac{b}{2}}^{x_0 + \frac{b}{2}} Y_J(x) \sum_n X_n(x^s) X_n(x) dx \right| \\ &\simeq \left| \int_{x_0 - \frac{b}{2}}^{x_0 + \frac{b}{2}} Y_J(x) \delta(x - x^s) dx \right| \\ &= |Y_J(x^s)|.\end{aligned}\tag{5.18}$$

Now, if we consider the following orthonormal basis of $L^2[x_0 - b/2, x_0 + b/2]$

$$Y_j(x) = \sqrt{\frac{2}{b}} \sin \left(\frac{(x^s - x_0 + \frac{b}{2})j\pi}{b} \right), \quad j = 1, 2, \dots, \tag{5.19}$$

(5.18) implies that

$$\tilde{\mathcal{I}}_J^{KM}(\vec{y}^s) = \frac{2}{b} \sin^2 \left(\frac{(x^s - x_0 + \frac{b}{2})J\pi}{b} \right). \tag{5.20}$$

In the following section, we will compare this result with the outcome of our numerical simulations.

5.3 Comparison

In this section we compare the results of the previous chapter where the scatterer was a square, with those obtained for the simplified model of the present chapter where the scatterer is a vertical crack. Specifically, in the case where the scatterer is the crack, we will a) compare the results between selective imaging with $\tilde{\mathcal{I}}_J^{KM}$ and those obtained with the use of the asymptotic formula (5.20), and b) compare results between selective imaging with $\tilde{\mathcal{I}}_J^{KM}$ and \mathcal{I}_J^{KM} . Finally, we close this section comparing the results we get for the square scatterer using selective imaging with $\tilde{\mathcal{I}}_J^{KM}$, with the corresponding ones for the crack.

In all the following examples the sound speed will be taken equal to $c_0 = 1500$ m/s and the depth of the waveguide equal to $D = 200$ m.

5.3.1 $\tilde{\mathcal{I}}_J^{KM}$ vs. asymptotics

Let us consider a crack of length $b = 40$ m centered at $(450, 100)$ m, and a single frequency $f_0 = 75$ Hz for which the wavelength $\lambda_0 = 20$ m (thus the width of the crack here equals to $2\lambda_0$). The number of modes which propagate in the waveguide is $M = 20$. The theoretical results of Section 5.1 predict that the $M \times M$ principal part of the matrix A and, consequently, of the matrix $\hat{\mathbb{P}}$, defined in (5.3) and (5.8), respectively, have $\lceil \frac{2b}{\lambda} \rceil = 4$ significant singular values. In Figure 5.2 we plot the singular values of the 20×20 principal submatrix of A (left subplot) normalized with respect to the largest one. In the middle subplot of Figure 5.2, we plot the normalized singular values of $\hat{\mathbb{P}}$ which, as predicted from the theory, are identical to those of A . In the right subplot, we plot the singular values of the array response matrix $\hat{\Pi}$, see (5.2), (5.4).

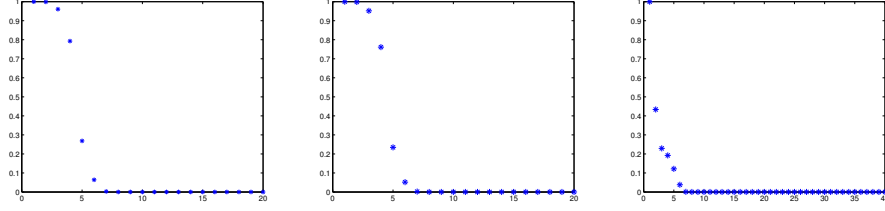


Figure 5.2: Singular value distribution for A (left), $\hat{\mathbb{P}}$ (middle) and $\hat{\Pi}$ (right), normalized w.r.t the largest singular value, for $b = 40$ m, $D = 200$ m, $c_0 = 1500$ m/s, $f_0 = 75$ Hz.

Let us comment that although the asymptotic analysis performed in the previous sections infers that the singular values of A and $\hat{\mathbb{P}}$ are either 0 or 1, we do not expect this to hold in the case of a fixed n , but we rather expect to be able to characterize as significant, the singular values which lie above some certain threshold. As one can immediately see in Figure 5.2 it is easy to distinguish the first four singular values of the matrices A and $\hat{\mathbb{P}}$ from the rest, while this is not the case for the singular values of $\hat{\Pi}$.

We now turn to checking the validity of the asymptotic expression (5.20). In Figures 5.3–5.6 the blue curve depicts the graph of $\tilde{\mathcal{I}}_J^{KM}(\vec{x}^s)$, given in (3.24), for \vec{x}^s located at the correct range L . The subscript J indicates that only the J -th singular vector is employed in the filtered version of the matrix $\hat{\mathbb{P}}$, defined in (5.8). The red line depicts the graph of (5.20). Specifically, Figure 5.3 illustrates the results concerning filtering with the first singular vector. As one may immediately see there is an excellent agreement between the numerics and the asymptotic expression. The same conclusion may also be drawn from Figure 5.4, where the filtering was done by means of the second singular vector ($J = 2$).

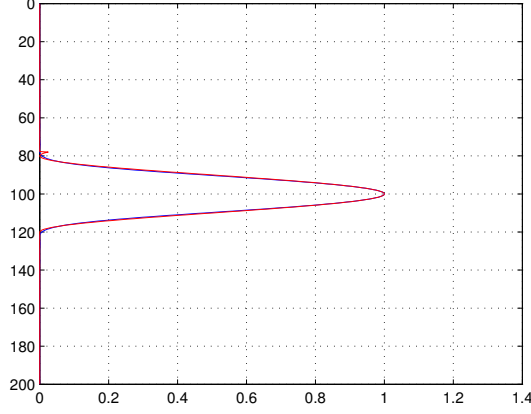


Figure 5.3: Values of $\left|\tilde{\mathcal{I}}_1^{KM}\right|$ on the crack (blue line) versus values obtained by asymptotics in (5.20) for $J = 1$ (red line), for $b = 40$ m, $D = 200$ m, $c_0 = 1500$ m/s, $f_0 = 75$ Hz.

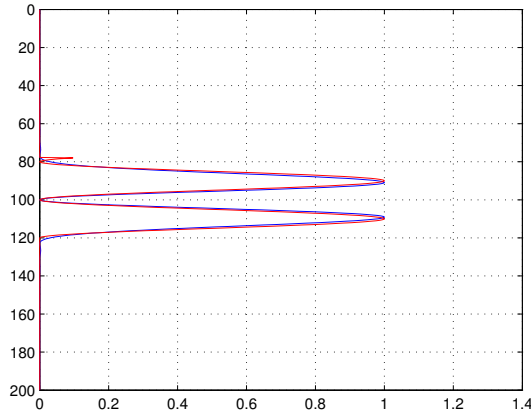


Figure 5.4: Values of $\left|\tilde{\mathcal{I}}_2^{KM}\right|$ on the crack (blue line) versus values obtained by asymptotics in (5.20) for $J = 2$ (red line), for $b = 40$ m, $D = 200$ m, $c_0 = 1500$ m/s, $f_0 = 75$ Hz.

The corresponding results for selective imaging based on the third and the fourth singular vectors are shown in Figures 5.5 and 5.6, respectively. In these one may notice some discrepancy between the asymptotic expression and the numerical result. This may be attributed to the fact that the asymptotic

analysis is based on matrices of order n , where $n \rightarrow \infty$, while in the numerics only their $M \times M$ part has been taken into account. For example, the orthogonality of the \vec{a}_i defined in (5.14) is valid only when A is an infinite matrix and is expected to hold only approximately for fixed n .

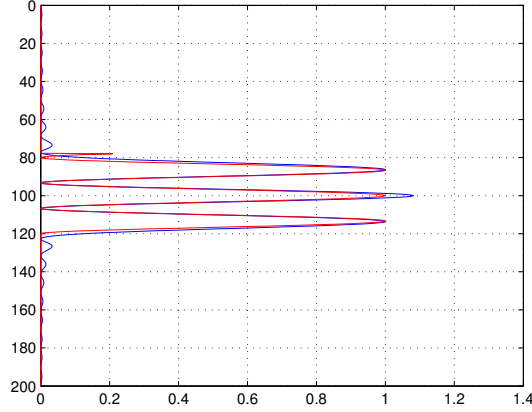


Figure 5.5: Values of $|\tilde{\mathcal{I}}_3^{KM}|$ on the crack (blue line) versus values obtained by asymptotics in (5.20) for $J = 3$ (red line), for $b = 40$ m, $D = 200$ m, $c_0 = 1500$ m/s, $f_0 = 75$ Hz.

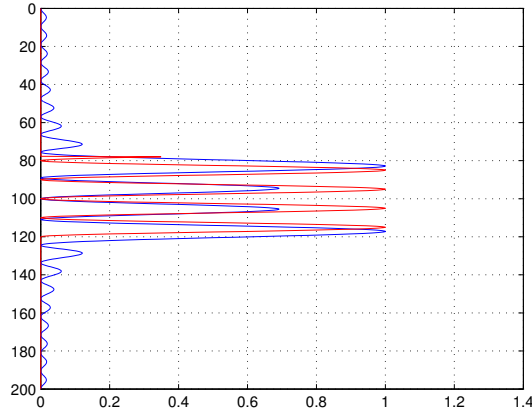
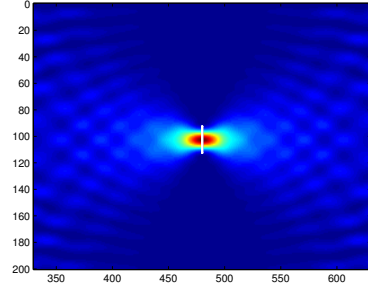
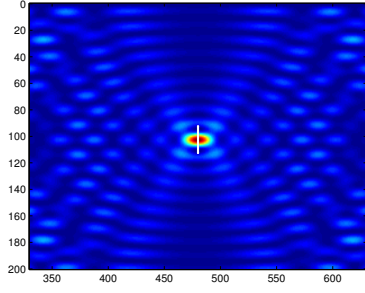


Figure 5.6: Values of $|\tilde{\mathcal{I}}_4^{KM}|$ on the crack (blue line) versus values obtained by asymptotics in (5.20) for $J = 4$ (red line), for $b = 40$ m, $D = 200$ m, $c_0 = 1500$ m/s, $f_0 = 75$ Hz.

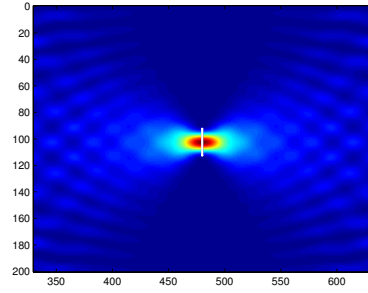
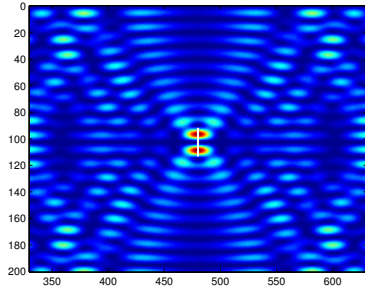
5.3.2 \mathcal{I}_J^{KM} vs. $\tilde{\mathcal{I}}_J^{KM}$

In this section we compare our results concerning selective imaging with \mathcal{I}_J^{KM} and $\tilde{\mathcal{I}}_J^{KM}$. Specifically, we consider a crack of width $b = 20$ m and we plot in the left column of Figure 5.7 the modulus of $\mathcal{I}_1^{KM}(\vec{x}^s)$ and in the right one the modulus of $\tilde{\mathcal{I}}_1^{KM}(\vec{x}^s)$, for frequencies $f = 73, 75, 79$, and 81 Hz (top to bottom). The subscript 1 indicates that both matrices $\hat{\Pi}$ and $\hat{\mathbb{P}}$, which are employed in the computation of \mathcal{I}_J^{KM} and $\tilde{\mathcal{I}}_J^{KM}$, respectively, are filtered using the first singular vector.

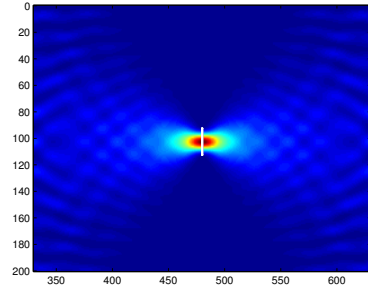
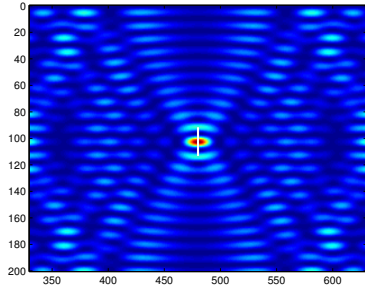
In the right column of Figure 5.7, for all four frequencies, we recognize the expected behavior of the selective imaging with $\tilde{\mathcal{I}}_1^{KM}$, based on the first singular vector of the matrix $\hat{\mathbb{P}}$. As we have shown in (5.9), the matrix $\hat{\mathbb{P}}$ is unitarily equivalent to A , which means that the singular values of both matrices are the same (modulo some multiplicative constant). On the other hand, the matrix A is related to the array response matrix $\hat{\Pi}$ via the relation (5.7), which implies a rather complicated dependence between their SVD's. As a result in the left column of Figure 5.7 we meet the expected behavior of the selective imaging with \mathcal{I}_1^{KM} , based on the first singular vector of the matrix $\hat{\Pi}$, for frequencies $f = 73$ and 79 Hz shown in the first and third row, respectively, but not for frequencies $f = 75$ and 81 Hz, which are shown in the second and fourth row, respectively. This lack of robustness has motivated us to work with $\tilde{\mathcal{I}}^{KM}$ rather than with \mathcal{I}^{KM} .



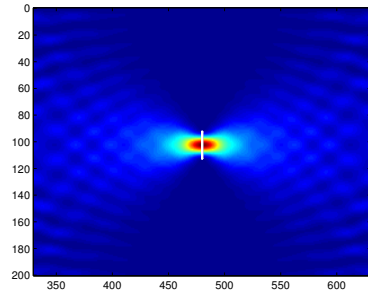
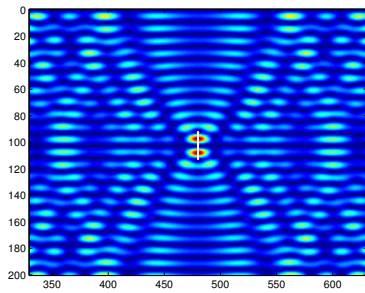
$f_0 = 73$ Hz.



$f_0 = 75$ Hz.



$f_0 = 79$ Hz.



$f_0 = 81$ Hz.

Figure 5.7: Values of $|Z_1^{KM}|$ (left column) and $|\tilde{Z}_1^{KM}|$ (right column), for $b = 20$ m, $D = 200$ m, $c_0 = 1500$ m/s, when projecting on the first singular vector, for frequencies $f_0 = 73, 75, 79$ and 81 Hz.

5.3.3 Full object vs. crack

Now, let us compare the results we get when we use selective imaging with $\tilde{\mathcal{I}}^{KM}$ when the scatterer is a square, with the corresponding ones for the crack. The side length of the square and the width of the crack was taken equal to $b = 40$ m. In both cases, we used broadband illumination with bandwidth $B = 10$ Hz and central frequency $f_0 = 75$ Hz.

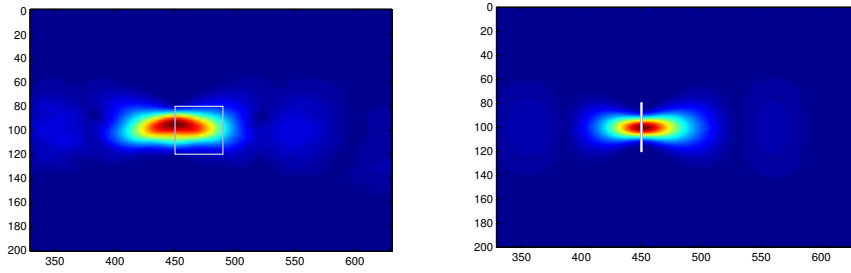
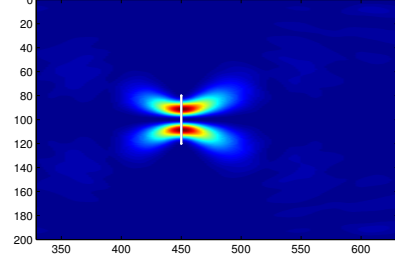
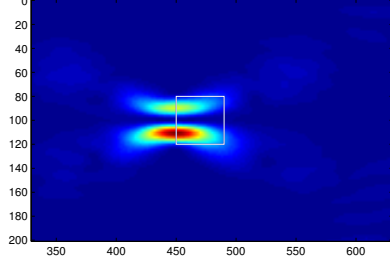


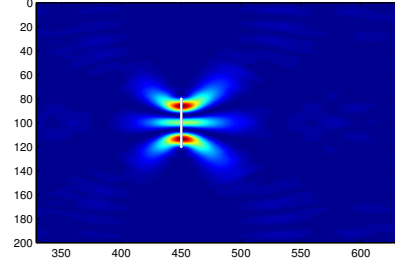
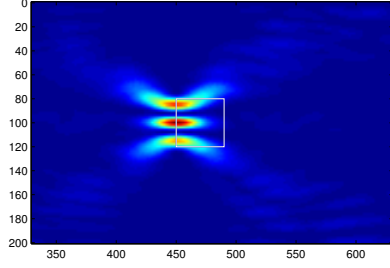
Figure 5.8: Values of $\tilde{\mathcal{I}}_1^{KM}$ for the square scatterer (left subplot) and for the crack (right subplot), for $b = 40$ m, $D = 200$ m, $c_0 = 1500$ m/s, $f_0 = 75$ Hz, $B = 10$ Hz.

In Figure 5.8 we see that when we project on the first singular vector, both images seem to focus on the center of the object. This is something that we have already seen for the crack. The fact that the image for the square scatterer behaves similarly verifies our intuition that the signals we collect on our receivers carry the information which mostly stem from the left side of the object.

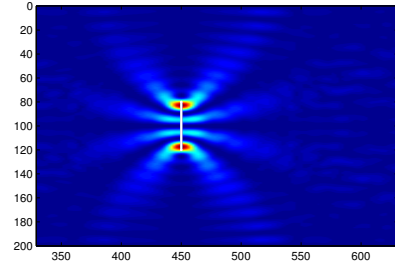
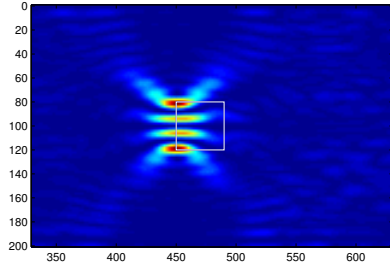
The same good agreement is shown in Figure 5.9, where the first, second and third rows correspond to the results obtained when we project on the second, third and fourth singular vectors, respectively.



$J = 2$



$J = 3$



$J = 4$

Figure 5.9: Values of $\tilde{\mathcal{I}}_J^{KM}$ for the square scatterer (left subplot) and for the crack (right subplot), for $b = 40$ m, $D = 200$ m, $c_0 = 1500$ m/s, $f_0 = 75$ Hz, $B = 10$ Hz. J denotes the projection on the J -th singular vector.

Conclusion

In this thesis we considered the problem of selective imaging of extended reflectors in a waveguide using an active array of sensors. To this end, we proposed a novel selective imaging functional based on Kirchhoff migration and the singular value decomposition of $\hat{\mathbb{P}}(\omega)$, which is a normalized modal projection of the array response matrix. The theoretical analysis of our imaging method was carried out using a simplified model for the reflector. The following main results were obtained:

1. We showed that the rank of $\hat{\mathbb{P}}(\omega)$ is equal to $\lfloor \frac{b}{\lambda/2} \rfloor$, that is, the size of the reflector, b , divided by the array resolution, $\lambda/2$ (λ being the wavelength at frequency ω). This result has been proven recently in free space (cf. [4, §4.5.2]), but, to the best of our knowledge, it is a new result for waveguides.
2. We derived analytic expressions for the singular vectors of $\hat{\mathbb{P}}(\omega)$, as well as for our selective imaging functional. Exploiting these expressions we showed that imaging using the projection of $\hat{\mathbb{P}}(\omega)$ on its first singular vector results to an image focused at the center of the reflector, while projecting on the last significant singular vector focuses the image at the boundary of the reflector. Again our results are similar to the ones obtained in free space (cf. [4]).

The numerical results we have acquired are in very good agreement with our theoretical results.

One of the main assumptions in the analysis was that the array spans the whole waveguide, a hypothesis that is probably not realistic for applications. It would be therefore of great interest to generalize these results to the case

of partial array aperture. This does not seem at all straightforward. Without the array spanning the whole waveguide, we lose properties such as the orthonormality of the vertical eigenfunctions X_n across the array.

At this point, let us note that while all the analytical results were obtained under the assumption of a Dirichlet boundary condition on the bottom, everything carries over to the case of a Neumann boundary condition.

Bibliography

- [1] Montjoie user's guide. <http://montjoie.gforge.inria.fr/>.
- [2] J.-P. Berenger. A perfectly matched layer for the absorption of electromagnetic waves. *Journal of Computational Physics*, 114:185 – 200, 1994.
- [3] N. Bleistein. *Mathematical methods for wave phenomena*. Computer Science and Applied Mathematics. Academic Press Inc., Orlando, FL, 1984.
- [4] L. Borcea, G. Papanicolaou, and F. Guevara Vasquez. Edge illumination and imaging of extended reflectors. *SIAM J. Imaging Sci.*, 1:75–114, 2008.
- [5] L. Borcea, G. Papanicolaou, and C. Tsogka. Optimal illumination and waveform design for imaging in random media. *J. Acoust. Soc. Am.*, 122:3507–3519, 2007.
- [6] L. Borcea, G. Papanicolaou, and C. Tsogka. Subspace projection filters for imaging in random media. *Comptes Rendus Mecanique*, 338:390–401, 2010.
- [7] D. Fasino. Spectral properties of Toeplitz-plus-Hankel matrices. *Calcolo*, 33:87–98, 1996.
- [8] S.D. Gedney. An anisotropic perfectly matched layer-absorbing medium for the truncation of FDTD lattices. *IEEE Transactions on Antennas and Propagation*, 44:1630 –1639, 1996.

- [9] G. H. Golub and C. F. Van Loan. *Matrix computations*. Johns Hopkins Studies in the Mathematical Sciences. Johns Hopkins University Press, Baltimore, MD, third edition, 1996.
- [10] R. M. Gray. Toeplitz and circulant matrices: A review. Technical report, Information Systems Laboratory Technical Report, Stanford University, 2001.
- [11] U. Grenander and G. Szegő. *Toeplitz forms and their applications*. Chelsea Publishing Co., New York, second edition, 1984.
- [12] C. Hazard and K. Ramdani. Selective acoustic focusing using time-harmonic reversal mirrors. *SIAM J. Appl. Math.*, 64:1057–1076 (electronic), 2004.
- [13] F.B. Jensen, W.A. Kuperman, M.B. Porter, and H. Schmidt. *Computational Ocean Acoustics*. Modern Acoustics and Signal Processing. Springer, 2011.
- [14] W.A. Kuperman and D. Jackson. Ocean acoustics, matched-field processing and phase conjugation. Topics in Applied Physics, pages 43–97. Springer Berlin / Heidelberg, 2002.
- [15] C. M. Linton. The Green’s function for the two-dimensional Helmholtz equation in periodic domains. *J. Engrg. Math.*, 33:377–402, 1998.
- [16] B. Pinçon and K. Ramdani. Selective focusing on small scatterers in acoustic waveguides using time reversal mirrors. *Inverse Problems*, 23:1–25, 2007.
- [17] C. Prada, J. de Rosny, D. Clorennec, J.-G. Minonzio, A. Aubry, M. Fink, L. Berniere, P. Billand, S. Hibrat, and T. Folegot. Experimental detection and focusing in shallow water by decomposition of the time reversal operator. *J. Acoust. Soc. Amer.*, 122:761–768, 2007.
- [18] C. Prada and M. Fink. Eigenmodes of the time reversal operator: a solution to selective focusing in multiple-target media. *Wave Motion*, 20:151–163, 1994.

- [19] C. Prada, N. Mordant, and M. Fink. Highly resolved detection in a waveguide with the D.O.R.T. method. *J. Acoust. Soc. Amer.*, 105:1105–1105, 1999.
- [20] W. D. Wilson. Equation for the speed of sound in sea water. *J. Acoust. Soc. Amer.*, 32:1357–1357, 1960.
- [21] H. Zhao. Analysis of the response matrix for an extended target. *SIAM J. Appl. Math.*, 64:725 – 745, 2004.